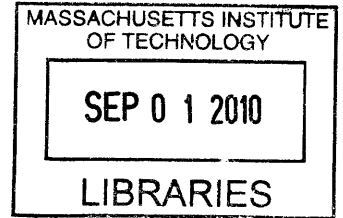


Influence of Induced Natural Convection on Laser
Propagation - Analysis and Interferometric
Visualization

by
Aditya Bhakta

B.Tech., Indian Institute of Technology Bombay (2005)



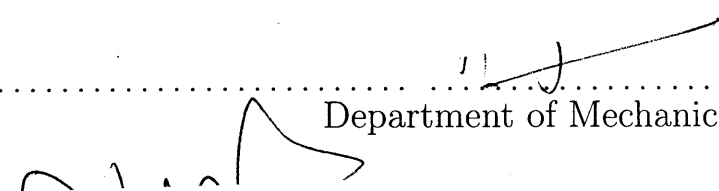
ARCHIVES

Submitted to the Department of Mechanical Engineering in partial
fulfillment of the requirements for the degree of


Master of Science in Mechanical Engineering
at the
MASSACHUSETTS INSTITUTE OF TECHNOLOGY
June 2010

© Massachusetts Institute of Technology 2010. All rights reserved.

Author


Department of Mechanical Engineering
May 07, 2010

Certified by


George Barbastathis
Associate Professor
Thesis Supervisor

Accepted by


David E. Hardt
Chairman, Department Committee on Graduate Theses

Influence of Induced Natural Convection on Laser Propagation - Analysis and Interferometric Visualization

by

Aditya Bhakta

Submitted to the Department of Mechanical Engineering on May 07, 2010
in partial fulfillment of the requirements for the degree of
Master of Science in Mechanical Engineering

Abstract

This thesis analyzes the influence of a self-induced natural convection flow on the propagation of a high energy laser beam. The two configurations considered are of a vertical laser beam (propagation direction opposite to gravity) and a horizontal laser beam (gravity acting in a direction perpendicular to propagation) travelling through an infinite expanse of quiescent fluid. Hamiltonian optics is used to predict the evolution of rays at steady state. The change in refractive index due to localized heating of the fluid by the laser is measured using interferometry.

For the vertical laser beam, one model considers the beam to be a linear energy source. Another model considers the spatial intensity distribution of the beam as a generation term in the energy conservation equation. Simulation for both the models predict the formation of a caustic, as the beam propagates through the medium. Due to radial symmetry, there is a dense packing of rays along the periphery of a circle. Here, this formation is referred to as the *thermal ring*. The horizontal laser beam is first modeled as a linear source of uniform strength along the propagation path. The change in temperature is calculated using a similarity solution, and the resulting refractive index change predicts the ray behaviour. Here again, formation of a caustic is suggested, with a high density of the rays at two locations above the beam centre. Modeling of the laser as a decaying line source also predicts the densing of rays.

The thermal lensing caused by a horizontal 120mW laser in a 1% aqueous Toluidine Blue sample is visualized using a Mach-Zehnder interferometer. The interferograms are analyzed using both the Fourier methods and phase shifting. Both predict the change in refractive index near the beam to be of the same order of magnitude as the simulation results.

Thesis Supervisor: George Barbastathis
Title: Associate Professor

Acknowledgment

I take this opportunity to thank my advisor - Professor George Barbastathis, for having the belief in my capabilities and guiding me through this research, while providing all the support possible. I specially appreciate his patience and encouragement during the initial semesters at MIT. Coming off a break from academic studies, this has instilled confidence in me, and spurred me on for active research.

It is also my pleasure to thank all my group members for their suggestions and discussions. It would only be fair to specially mention Se Baek Oh, Nick Loomis, Jose A. Dominguez-Caballero, Laura A. Waller and Lei Tian for their continuous help and insight. I also thank Yuan Luo and Nader Shaar for their help. I would also like to express my gratitude to all my friends at MIT for creating memorable moments and making me feel at home away from home.

I also thank my friends Harish, Shiva, Mehul, Anshul and Mohit, back home in India for being there in the good and not-so-great times. Finally, words would just not suffice thanking the unending love, support and encouragement from my parents. They have been my first teachers and learning has never stopped.

Contents

1	Introduction	15
1.1	Thesis Outline	16
1.2	Geometrical Optics	17
1.2.1	Ray Hamiltonian	18
1.2.2	The Screen Hamiltonian	21
1.3	Natural Convection	23
1.3.1	The Conservation Equations	23
1.3.1.1	Conservation of Mass	24
1.3.1.2	Conservation of Momentum	24
1.3.1.3	Conservation of Energy	25
1.3.2	Boussinesq Approximation	25
1.3.3	Buoyancy Force and Thermal Coupling	26
1.3.4	Steady State Formulation	28

1.3.5	Boundary Layer Approximations	29
1.4	Interferometry	31
1.4.1	The Mach-Zehnder Interferometer	32
1.4.2	Interferogram Analysis	33
1.4.2.1	Fourier Transform Methods	34
1.4.2.2	Phase Shifting Methods	35
2	Vertical Laser Beam	37
2.1	Line Source Model	38
2.2	Intensity as Generation Term	42
2.2.1	Governing Equations	43
2.2.2	Similarity Solution	45
2.2.3	Refractive Index Profile	46
2.2.4	Ray Evolutions	48
3	Horizontal Laser Beam	53
3.1	Laser Propagation in a Cross-flow	54
3.2	Uniform Line Source	60
3.2.1	Governing Equations	60
3.2.2	Similarity Solution	62

3.2.3	Ray Evolution	64
3.3	Decaying Line Source	69
4	Interferometric Visualization	77
4.1	Experimental Setup	78
4.2	Observations	80
4.3	Interferogram Analysis	82
4.4	Comparison with Simulations	91
4.5	Dye Alternatives	95
5	Conclusion	99
A	Livingston Parameter β	105
B	Convection ODEs and Approximation Validity	107

List of Figures

1.1	The Eikonal.	19
1.2	The ray momentum.	20
1.3	The Screen Hamiltonian.	22
1.4	The Mach-Zehnder Interferometer.	33
2.1	The vertical uniform line source model.	39
2.2	Vertical ray evolution.	41
2.3	The ray pattern evolution for circular grids.	42
2.4	The decaying intensity model setup for vertical beam	43
2.5	Temperature Profile for the Vertical Beam in water at 300K	47
2.6	Normalized Refractive Index Profile. $\{n^* = (n/n_0) \times 10^4\}$	49
2.7	The ray pattern evolution for a vertical beam.	51
3.1	The Livingston model for natural convection.	55

3.2	Intensity profile and corresponding isocontour lines along beam propagation axis.	57
3.3	Ray Pattern at different propagation distance for forced convection	59
3.4	The uniform horizontal line source model	61
3.5	Temperature excess ($T - T_\infty$) in the XY plane for a uniform horizontal line source.	65
3.6	Refractive Index in the XY plane for a uniform horizontal line source.	66
3.7	Ray pattern for a 0.001m circular grid.	67
3.8	Ray pattern for multiple circular grids ($r = 0.6\text{mm}, 0.7\text{mm}, 0.8\text{mm}, 1.0\text{mm}, 1.2\text{mm}$ and 1.4mm).	68
3.9	The decaying line source model.	70
3.10	Refractive Index (XY) profile for the decaying line source at $z = 1\text{m}$	72
3.11	Ray evolution for a $r = 8\text{mm}$ circular grid (decaying line source). 74	
3.12	Ray pattern for multiple circular grids ($r = 8\text{mm}, 9\text{mm}, 10\text{mm}$). 75	
4.1	The Experimental Setup.	79

4.2	Interferograms (entire pixel area on the left and area near the beam on the right) for a Toluidine Blue sample heated by a 120mW beam.	81
4.3	The interferogram in Fourier domain with one side spot highlighted.	83
4.4	The Fourier method for interferogram analysis.	84
4.5	Evolution of the change in refractive index with time.	86
4.6	Evolution of centre-line change in refractive index with time	88
4.7	Centre-line change in refractive index at beam entry and steady state.	89
4.8	Phase difference due to laser heating - comparing original image data with <i>Hanning</i> and <i>Blackmann-Harris</i> windowed image.	90
4.9	Comparing the centre-line refractive index change from Fourier Method analysis of original image with <i>Hann</i> and <i>Blackman-Harris</i> windowed images.	92
4.10	Change in refractive index around the beam using Fourier method and PSM.	92
4.11	Simulation result for change in refractive index (uniform line source model).	93

4.12 Comparing the centre-line refractive index change estimated by simulations with the experimental results (spatial distance units in m).	94
4.13 Comparing the centre-line change in refractive index for Tolu- idine Blue and Malachite Green at steady state.	96
B.1 The error term	109

Chapter 1

Introduction

The propagation of a high energy laser beam depends on its interaction with the medium through which it travels. The region near the beam heats up, and as the energy is dissipated through the medium, a refractive index profile evolves. The redistribution of the beam intensity profile and the deviation of the beam path due to this self-induced change in refractive index is called Thermal Blooming. Depending on the response of the medium, there could be a defocusing of the beam - reducing the peak intensity at a desired target, or a focusing effect leading to formation of caustics. The nonlinear nature of this phenomenon has aroused a lot of theoretical interest [1-11] and with the advent of high energy lasers a lot of literature pertaining to propagation in the atmosphere exists [12-14]. The work however is limited to considering conduction and forced convection for heat dissipation. If the medium is a fluid, initially undisturbed, absorption of energy near the beam causes density

gradients to exist. If these overcome the gravitational body forces, the fluid is set in motion and a natural convection field is setup. Depending on the medium and resulting flow conditions, there could also be a possibility of waveguiding. Due to the complexity and high nonlinearity of this coupling, however, investigations have been limited to experimental verification and approximating the physics. This thesis analyzes the influence of such a self-induced natural convection flow on the propagation of a high power laser beam.

1.1 Thesis Outline

As mentioned, the evolution of a laser beam through a quiescent fluid medium depends on the mode of heat dissipation. For natural convection then, the refractive index profile needs to be evaluated considering the heat transfer and fluid dynamics involved. The behaviour of this light beam in such a refractive index distribution can then be analyzed by the geometrical optics formulation, and a possibility of beam defocusing or caustic formation can be investigated. Under practical laser strengths, the temperature differences caused in a fluid due to convection are of a small order of magnitude and interferometry can be used for visualization. The rest of this chapter discusses the principles of geometrical optics, natural convection and interferometry that were used in this body of work.

Two configurations of beam propagation are considered in this thesis. Chap-

ter 2 considers the case of a vertical laser beam, propagating in an undisturbed medium in the direction opposite to gravity. The steady state refractive index profile is calculated based on two physical models of the scenario. Ray path through such an index distribution is evaluated.

Chapter 3 pertains evolution of a horizontal laser beam propagating through a fluid medium, with gravity in a direction perpendicular to beam axis. Simulation of ray paths is again carried out by formulating two different physical models, where the beam is considered to be a linear energy source.

Chapter 4 presents the experimental results of using interferometry to visualize phase changes caused by laser traveling horizontally in a fluid sample. The results are compared with simulations using the uniform line source model.

The thesis concludes with Chapter 5 where a summary of the models used is outlined along with directions for future work.

1.2 Geometrical Optics

The behaviour of light is characterized by rapid oscillations of the electric and magnetic field. It is thus an electromagnetic wave and the propagation of this disturbance is described by the Maxwell's equations. The wavelength at optical frequencies however, is small ($\sim 4.7 \times 10^{-7}\text{m}$) and in cases where the length scales are several orders of magnitude larger than the wavelength, the wave nature can be neglected. Light propagation under this approxi-

mation is explained by ray trajectories and this approach is therefore called Geometrical optics. Physically speaking, ray paths are the directions along which energy is transported. The Hamiltonian method is a tool to derive ray trajectories under the geometrical optics approximation in non-uniform media - i.e. media with a non-uniform refractive index.

1.2.1 Ray Hamiltonian

Analogous to the Hamiltonian formulation in dynamics, Hamiltonian equations for a ray describe propagation through a medium. A simple approach of arriving at the ray Hamiltonians from Snell's law, which is a conservation law for the ray momentum, is outlined in [15]. Another approach says that the Hamiltonian equations follow directly based on two postulates for the ray behaviour [16]. In what follows, it is shown that the postulates are a direct consequence of the Eikonal equation.

In the limit of the wavelength being negligible, Maxwell's equations lead to the Eikonal equation [17]. This equation states that the wavefront \mathcal{S} - the surface normal to a ray bundle, and also called the eikonal - satisfies

$$\left(\frac{\partial\mathcal{S}}{\partial x}\right)^2 + \left(\frac{\partial\mathcal{S}}{\partial y}\right)^2 + \left(\frac{\partial\mathcal{S}}{\partial z}\right)^2 = n^2 \quad (1.2.1)$$

Here, $n(x, y, z)$ is the refractive index at a point, The eikonal $\mathcal{S}(x, y, z) = \text{constant}$ is interpreted as the geometrical wavefront (*Figure 1.1*). The main

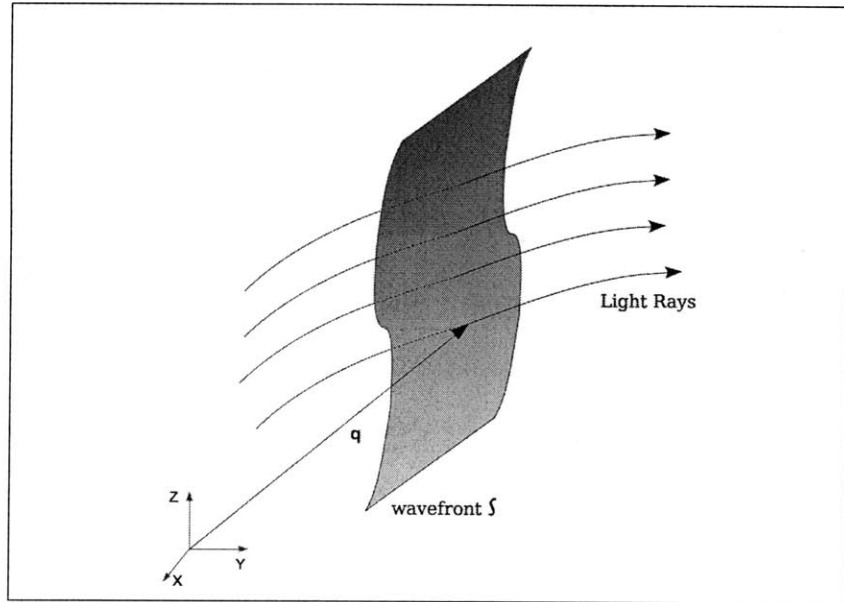


Figure 1.1: The Eikonal.

result that follows is that energy transport occurs in a direction given by the unit vector

$$\mathbf{s} = \frac{\nabla S}{n} \quad (1.2.2)$$

Thus if a ray is defined as the curve orthogonal to the geometric wavefront, the unit vector that is tangent to such a curve at a point $\mathbf{q}(s)$, here parameterized in terms of the arc length s , is \mathbf{s} and so

$$n \frac{d\mathbf{q}}{ds} = \nabla S \quad (1.2.3)$$

Now if a vector \mathbf{p} is defined to be the ray momentum and directed along the

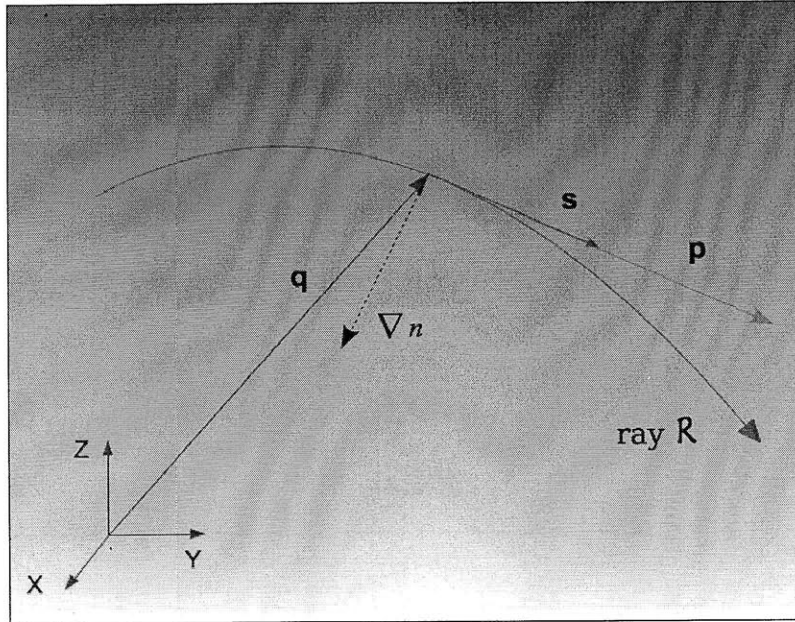


Figure 1.2: The ray momentum.

direction of \mathbf{s} (*Figure 1.2*) we have

$$\frac{d\mathbf{q}}{ds} = \frac{\mathbf{p}}{|\mathbf{p}|} \quad (1.2.4)$$

This is the first postulate - the geometrical postulate - which states that the rays are continuous and piecewise differentiable everywhere. Further, taking the derivative of *Equation 1.2.3* with respect to the arc length s we have

$$\frac{d}{ds} \left(n \frac{\mathbf{p}}{|\mathbf{p}|} \right) = \nabla n \quad (1.2.5)$$

Now defining a function H such as

$$H = |\mathbf{p}| - n(\mathbf{q}) = 0 \quad (1.2.6)$$

leads to the second 'dynamical postulate' which states that the momentum changes along the arc length is equal (by the choice of the function H here) to the local refractive index gradient; i.e.

$$\frac{d\mathbf{p}}{ds} = \nabla n \quad (1.2.7)$$

The function H is called the ray hamiltonian as *Equations 1.2.4, 1.2.6 and 1.2.7* lead to the following set of Hamiltonian equations:

$$\frac{d\mathbf{q}}{ds} = \frac{\partial H}{\partial \mathbf{p}}, \quad (1.2.8)$$

$$\frac{d\mathbf{p}}{ds} = -\frac{\partial H}{\partial \mathbf{q}} \quad (1.2.9)$$

1.2.2 The Screen Hamiltonian

The Hamiltonian equations are a 6×6 system and this can be reduced to a 4×4 system of equations by introducing the concept of a Screen Hamiltonian [16]. The idea is to change the parametrization of the equations from the arc length s to the Cartesian co-ordinate z , which is along the direction of propagation of the ray. The Hamiltonian equations in the Cartesian system

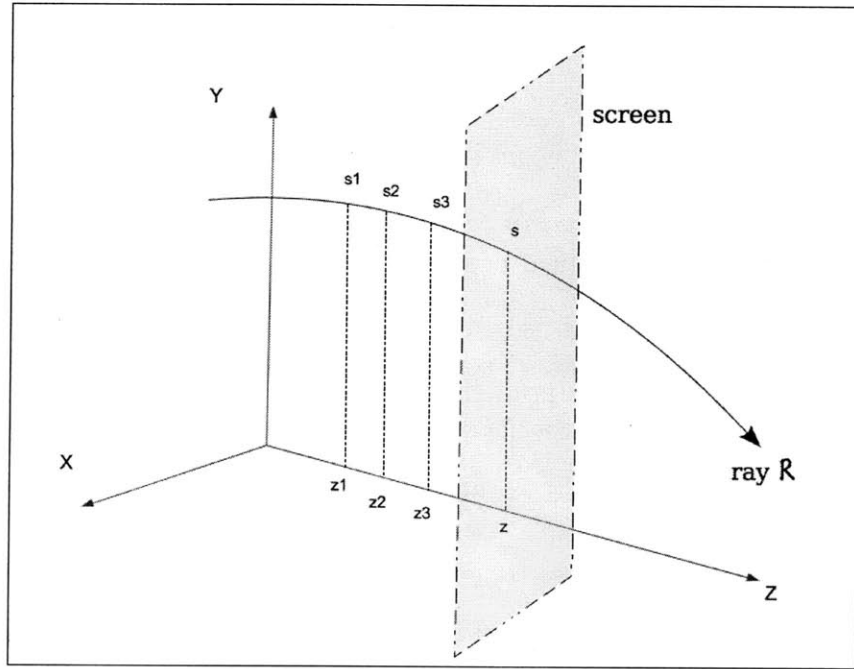


Figure 1.3: The Screen Hamiltonian.

are:

$$\begin{aligned} \frac{dq_x}{ds} &= \frac{\partial H}{\partial p_x}; & \frac{dp_x}{ds} &= -\frac{\partial H}{\partial q_x}, \\ \frac{dq_y}{ds} &= \frac{\partial H}{\partial p_y}; & \frac{dp_y}{ds} &= -\frac{\partial H}{\partial q_y}, \\ \frac{dq_z}{ds} &= \frac{\partial H}{\partial p_z}; & \frac{dp_z}{ds} &= -\frac{\partial H}{\partial q_z}, \end{aligned}$$

where q_x, q_y, q_z are components of \mathbf{q} and p_x, p_y, p_z are components of \mathbf{p} . Next, parameterizing with z by setting $q_z = z$ and using the chain rule

$$\frac{dq_x}{dz} = \frac{p_x}{p_z}; \quad \frac{dq_y}{dz} = \frac{p_y}{p_z}; \quad (1.2.10)$$

$$\frac{dp_x}{dz} = \frac{n}{p_z} \frac{\partial n}{\partial q_x}; \quad \frac{dp_y}{dz} = \frac{n}{p_z} \frac{\partial n}{\partial q_y} \quad (1.2.11)$$

Now defining a function $h = -p_z$ and using *Equation 1.2.6* we have

$$h = -\sqrt{n^2 - p_x^2 - p_y^2} \quad (1.2.12)$$

It then follows from *Equation 1.2.10* and *1.2.11* that

$$\frac{dq_x}{dz} = \frac{\partial h}{\partial p_x}; \quad \frac{dp_x}{dz} = -\frac{\partial h}{\partial q_x} \quad (1.2.13)$$

$$\frac{dq_y}{dz} = \frac{\partial h}{\partial p_y}; \quad \frac{dp_y}{dz} = -\frac{\partial h}{\partial q_y} \quad (1.2.14)$$

These are called the *Screen Hamiltonian* equations, the function h being the *Screen Hamiltonian*. This is because these equations describe the evolution of the intersection of rays with planes (called as “screens”) perpendicular to the optical axis Z .

1.3 Natural Convection

1.3.1 The Conservation Equations

The analysis of a convection problem starts with the conservation of physical quantities of interest for the smallest fluid element. For the convection case, these are essentially the mass, momentum and energy conservation. The different variables involved are linked together by physical laws called the

constitutive relations. Based on these constitutive relations, the general conservation equations govern the phenomena under consideration. The general approach then is to simplify these equations based on different assumptions.

1.3.1.1 Conservation of Mass

Considering a small control volume in space for which the net inflow rate of fluid will be equal to the rate of mass generation within, in accordance with mass conservation, the mass continuity equation is:

$$\frac{D\rho}{Dt} = -\rho\nabla \cdot \mathbf{v} \quad (1.3.1)$$

Here ρ is the fluid density and \mathbf{v} the fluid velocity at a point and D/Dt is the substantial derivative. For the case of an incompressible fluid, mass conservation takes the form

$$\nabla \cdot \mathbf{v} = 0 \quad (1.3.2)$$

1.3.1.2 Conservation of Momentum

This essentially is equating the net force acting on a fluid element in space to the rate of change of momentum. Under the assumptions of a Newtonian viscous fluid (which gives the constitutive relation linking stress components to velocity gradients) and that the only body force acting is gravity, the

governing equation takes the form:

$$\rho \frac{D\mathbf{v}}{Dt} = -\nabla P + \rho \mathbf{g} + \mu \nabla^2 \mathbf{v} \quad (1.3.3)$$

Here P is the static pressure, \mathbf{g} the gravity vector and μ is the dynamic viscosity. The *second coefficient of viscosity/ bulk viscosity* has been neglected. This is a vector equation and is also known as the Navier-Stokes equation.

1.3.1.3 Conservation of Energy

Energy conservation states that the net rate of heat inflow in a volumetric fluid element must equal the rate of increase in thermal energy. Assuming a Newtonian fluid and incompressibility, the governing energy equation is:

$$\rho C_p \frac{DT}{Dt} = \nabla \cdot k \nabla T + \mu \Phi + \dot{Q}_v, \quad (1.3.4)$$

where C_p is the specific heat capacity, T is temperature, k is thermal conductivity of the fluid, $\mu \Phi$ is the viscous dissipation and \dot{Q}_v is the volumetric heat generation within the fluid.

1.3.2 Boussinesq Approximation

Boussinesq approximation is a set of approximations which further simplify the governing equations specified earlier. A formal discussion about the

validity of these assumptions can be found in most advanced fluid mechanics texts like [18]. The main simplifications are:

- The fluid can be considered incompressible.
- The change in fluid density is significant only in the force term appearing in the momentum conservation equation - *Equation 1.3.3*, and can be assumed constant elsewhere.
- The viscous dissipation term $\mu\Phi$ in *Equation 1.3.4* can be neglected.

An order of magnitude comparison of various terms in these equations determine the criteria under which the Boussinesq approximations hold true. It is required that the velocities involved are well below Mach number and there is no sudden change in the fluid density and pressure such as in the case of wave shocks or fluid motion involving large vertical distances. It is also required that the temperature variations be small.

The velocities and temperature changes involved in free convection are usually of a small magnitude. Hence, simplifying the governing equations with Boussinesq approximation is reasonable.

1.3.3 Buoyancy Force and Thermal Coupling

Driving fluid motion in natural convection are the density gradients that set in usually due to localized heating. This is evident with the appearance

of buoyancy force in the Navier-Stokes equation. The pressure term P in *Equation 1.3.3* is the static pressure; i.e., the pressure that would be measured by an observer moving with the fluid element. This could be considered to be a combination of two pressures - the hydrostatic pressure P_h and the motion pressure P_m [19]. The hydrostatic pressure is equivalent to the static pressure P when there is no fluid motion i.e. $\mathbf{v} = 0$. If there is no fluid motion, the medium is undisturbed and the density is equal to the ambient density ρ_∞ . So a definition for P_h from *Equation 1.3.3* is:

$$-\nabla P_h = -\rho_\infty \mathbf{g} . \quad (1.3.5)$$

The Navier-Stokes equation thus becomes

$$\rho \frac{D\mathbf{v}}{Dt} = -\nabla P_m + (\rho - \rho_\infty) \mathbf{g} + \mu \nabla^2 \mathbf{v} . \quad (1.3.6)$$

The term $(\rho - \rho_\infty) \mathbf{g}$ is the buoyancy force per unit volume that acts on a material element of density ρ placed in an ambient fluid at density ρ_∞ . Usually in external flows, the motion pressure gradient ∇P_m can be neglected. In the absence of pressure gradients, the density of fluid will be a function of temperature T and this signifies the coupling of the Navier-Stokes equation with the energy equation. Under these circumstances, for an ideal gas, it can

be shown that the volumetric thermal expansion coefficient β is given as

$$\beta = -\frac{1}{\rho} \frac{\partial \rho}{\partial T} . \quad (1.3.7)$$

This is found to be satisfied for most fluids as well if the temperature changes are not large. Dividing *Equation 1.3.6* throughout by ρ , with $\nu = \mu/\rho$ as the kinematic viscosity, the Navier-Stokes equation reduces to

$$\frac{D\mathbf{v}}{Dt} = -(\beta\Delta T)\mathbf{g} + \nu\nabla^2\mathbf{v} . \quad (1.3.8)$$

1.3.4 Steady State Formulation

The heating effect due to a laser is instantaneous and the system reaches a steady state fast. Experiments with a 120mW laser beam passing through a 2mm cell containing dyes like Toluidine Blue, Malachite Green etc. showed that a steady state was reached in around 3 seconds. Hence, the steady state configuration is considered here. The steady state momentum and energy equation for a fluid element based on the assumptions stated in the earlier sections are

$$\mathbf{v} \cdot \nabla \mathbf{v} = \mathbf{g}\beta\Delta T + \nu\nabla^2\mathbf{v} , \quad (1.3.9)$$

$$\rho C_p (\mathbf{v} \cdot \nabla T) = \nabla \cdot k\nabla T + \dot{Q}_v . \quad (1.3.10)$$

These coupled equations are used henceforth to describe the phenomenon of induced natural convection due to localized heating by a laser beam.

1.3.5 Boundary Layer Approximations

The Navier-Stokes equation is a nonlinear differential equation of order two. Analytical solutions can be found easily only for a few general cases. One of these is the low Reynolds number flow where the nonlinear inertia terms approach zero and there is a balance of the pressure and viscous forces. The other case is of inviscid flows where viscous forces approach zero and the system reduces to solving a linear Laplace equation. The Navier-Stokes equation for a 2D fluid element under the Boussinesq approximation is:

$$u \frac{\partial u}{\partial x} + v \frac{\partial u}{\partial y} = g\beta\Delta T + \nu \left(\frac{\partial^2 u}{\partial x^2} + \frac{\partial^2 u}{\partial y^2} \right) \quad (1.3.11)$$

Inertia *Buoyancy + Viscous*

The boundary layer is a region that contains the disturbance caused by the flow (velocity boundary layer) or heat source (thermal boundary layer). It is usually found in the characteristic plume formation of natural convection that the spatial extent of the boundary layer in one direction is orders of magnitude smaller than in the others. Consider the characteristic scale values for variables u, v, x, y to be U, V, L, δ . Here then $\delta \ll L$. Introduce u^*, v^*, x^*, y^* as the ratio of the variables and their corresponding scale values. By this definition $\mathcal{O}(u^*, v^*, x^*, y^*) \approx 1$. Now from the continuity equation $\mathcal{O}(v) \sim (\delta/L)U$. Using the new variables, the Navier-Stokes equation is:

$$\frac{U^2}{L} \frac{\partial u^*}{\partial x^*} + \frac{U^2}{L} \frac{\partial u^*}{\partial y^*} = g\beta\Delta T + \nu \left(\frac{U}{L^2} \frac{\partial^2 u^*}{\partial x^{*2}} + \frac{U}{\delta^2} \frac{\partial^2 u^*}{\partial y^{*2}} \right). \quad (1.3.12)$$

Simplifying and rearranging the terms on the right hand side,

$$\frac{\partial u^*}{\partial x^*} + \frac{\partial u^*}{\partial y^*} = \frac{g\beta\Delta TL^3}{\nu^2 (UL/\nu)^2} + \left(\frac{\nu}{U\delta}\right) \left(\frac{L}{\delta}\right) \left(\frac{\delta^2}{L^2} \frac{\partial^2 u^*}{\partial x^{*2}} + \frac{\partial^2 u^*}{\partial y^{*2}}\right). \quad (1.3.13)$$

Defining the nondimensional quantities $Gr_L = (g\beta\Delta TL^3/\nu^2)$ and $Re_x = (Ux/\nu)$ and since $(\delta/L) \ll 1$, above equation becomes

$$\frac{\partial u^*}{\partial x^*} + \frac{\partial u^*}{\partial y^*} = \frac{Gr_L}{Re_L^2} + \left(\frac{1}{Re_\delta}\right) \left(\frac{L}{\delta}\right) \left(\frac{\partial^2 u^*}{\partial y^{*2}}\right). \quad (1.3.14)$$

The terms on the left are $\mathcal{O}(1)$ and hence for the viscous and buoyancy terms to be of same order, the two requirements are

$$Re_\delta \gg 1, \quad (1.3.15)$$

$$\mathcal{O}(Gr_L) \sim \mathcal{O}(Re_L^2). \quad (1.3.16)$$

Under these conditions, the Navier-Stokes equation for the 2D element (reverting back to original variables) is

$$u \frac{\partial u}{\partial x} + v \frac{\partial u}{\partial y} = g\beta\Delta T + \nu \frac{\partial^2 u}{\partial y^2}. \quad (1.3.17)$$

Similarly, the energy equation is

$$\rho C_p \left(u \frac{\partial T}{\partial x} + v \frac{\partial T}{\partial y} \right) = k \frac{\partial^2 T}{\partial y^2} + \dot{Q}. \quad (1.3.18)$$

1.4 Interferometry

When two light waves coincide over a region, the intensity at a location depends on how the fields add together. This is the phenomenon of interference. If two waves of same frequency are propagating in the same direction with their field vectors in the same plane, the intensity I at a point where they interfere is given by

$$I = I_1 + I_2 + 2\sqrt{I_1 I_2} \cos \Delta\phi \quad (1.4.1)$$

where I_1, I_2 are the individual beam intensities and $\Delta\phi$ is the phase difference between them. If the two beams start with the same phase, the phase difference between the two beams is due to the difference in their corresponding optical paths. The optical path (and hence the refractive index) of an unknown material can thus be evaluated by analyzing the interference pattern produced. The optical instruments employed for such purposes are called interferometers.

The simplest of interferometers would require two beams that interfere. Consider that the nature of the two beams is known before they enter the setup. If the behaviour of one beam - the reference beam - is known, the distortion of the other wave can be inferred from the resulting interference pattern by nulling out the (known) effect of the reference. As mentioned, this distortion could have been generated by a change in the optical path by introduction of

an unknown sample, or a change in a physical parameter (say temperature, pressure etc.) that affects the refractive index.

The easiest option to know the phase of the beams before they enter the setup is to generate them from a single source. The two methods used to do this are *amplitude division* and *wavefront division*. In amplitude division, two beams are generated from the same region of a wavefront whereas in wavefront division, two beams are produced from different regions of a wavefront. The Mach-Zehnder interferometer is a two-beam amplitude division interferometer usually employed in examining fluid flow, heat transfer and temperature profile measurements [20-23].

1.4.1 The Mach-Zehnder Interferometer

The Mach-Zehnder Interferometer consists of two arms/paths created by the setup shown in *Figure 1.4*. Usually a He-Ne laser source is used to produce a collimated beam that enters the optical system through a beam splitter. The incident beam is divided into two by the beam splitter BS1, and after traveling through the two arms these recombine at beam splitter BS2. The fringe pattern of the setup without any sample gives the reference phase difference introduced due to the optical setup. Once a sample is introduced in the arm BS1-M2-BS2, the interference pattern changes and this can be used to calculate the unknown sample parameters (length, refractive index, temperature profile etc.). The spacing between the fringes can be easily controlled

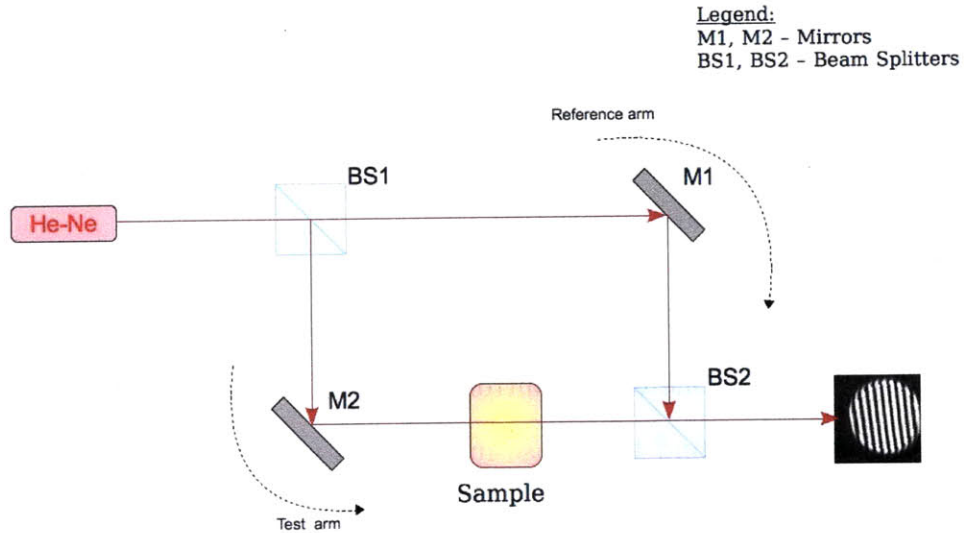


Figure 1.4: The Mach-Zehnder Interferometer.

by rotating either mirror. The location of the fringes can also be altered, to coincide with the sample for example, by changing the spacings between the components. The probe beam passes through the sample only once and this is useful when testing a highly distorting medium. The interferometer is very sensitive and hence finds wide applications in small phase change measurements - like convection flows, that are considered in this thesis. However it may be tricky to setup the interferometer to produce fringes in the first place and a good procedure to follow can be found in [25].

1.4.2 Interferogram Analysis

The fringe pattern (interferogram), from the interferometer is usually captured on a CCD camera. The phase information from the interferogram can

then be analyzed using various digital techniques. The two main methods are explained below.

1.4.2.1 Fourier Transform Methods

If considering the Mach-Zehnder interferometer illuminated by a plane wave, introducing a tilt in one of the mirrors produces background fringes. An elegant technique to find the phase information was suggested by Takeda [26]. The fringe pattern is considered to have a carrier frequency f_0 . If the setup is in the XZ plane and the tilt is about the Y axis, the intensity at a point on the interferogram is given by

$$I(x, y) = a(x, y) + b(x, y) \cos(2\pi f_0 x + \Delta\phi(x, y)) \quad (1.4.2)$$

$$= a + \frac{1}{2} (be^{i\Delta\phi}) e^{i2\pi f_0 x} + \frac{1}{2} (be^{i\Delta\phi})^* e^{-i2\pi f_0 x} \quad (1.4.3)$$

where $\Delta\phi(x, y)$ is the phase difference introduced by the sample and $a(x, y)$ and $b(x, y)$ are slow varying when compared to $\Delta\phi(x, y)$. Taking the Fourier transform with respect to x , the frequency domain representation of the interferogram is

$$\mathcal{J}(u, y) = A(u, y) + C(u - f_0, y) + C^*(u + f_0, y) \quad (1.4.4)$$

with three distinct bright spots - provided the carrier frequency is high enough to avoid aliasing. Shifting the pattern C to the origin (by means

of band-pass filtering) and taking an inverse Fourier transform gives the unknown phase information as

$$\Delta\phi(x, y) = \tan^{-1} \left(\frac{\text{Im}[c(x, y)]}{\text{Re}[c(x, y)]} \right). \quad (1.4.5)$$

The phase so determined is modulo 2π and an unwrapping algorithm needs to be applied to extract the continuous phase [26, 27, 30]. The technique is very accurate. Various improvements and precautions have been suggested in the literature [27-32]. The advantage of the Fourier method is that only a single interferogram is required and thus a time dependent phenomenon can be easily visualized in real time.

1.4.2.2 Phase Shifting Methods

Another technique to extract phase information is to use phase shifted interferograms. A minimum of four phase shifted interferograms would be required and the accuracy of the method can depend on the number of images used. The easiest way to introduce a phase shift in the Mach-Zehnder interferometer is to translate or rotate one mirror. Rotation however, also changes the carrier frequency slightly. The technique using four interferograms [34] is outlined below. Consider a sequence of four interferograms captured by introducing a phase shift of 90° every time, so that:

$$I_1(x, y) = a(x, y) + b(x, y) \cos\Delta\phi(x, y)$$

$$I_2(x, y) = a(x, y) + b(x, y) \cos(\Delta\phi(x, y) + 90^\circ)$$

$$I_3(x, y) = a(x, y) + b(x, y) \cos(\Delta\phi(x, y) + 180^\circ)$$

$$I_4(x, y) = a(x, y) + b(x, y) \cos(\Delta\phi(x, y) + 270^\circ)$$

Then it can be seen that

$$\tan \Delta\phi(x, y) = -\frac{I_2 - I_4}{I_1 - I_3} \quad (1.4.6)$$

The phase so determined is again modulo 2π and phase unwrapping is required. Some disturbances like the high-frequency noise cannot be removed though [33]. Also, the phase shifting mechanism has to be fast to visualize a fast transient process.

Chapter 2

Vertical Laser Beam

The evolution of a vertical laser beam heating a liquid is considered in this chapter. The beam enters a quiescent medium in a direction opposite to the direction of gravity. Thermal absorption of the beam energy by the fluid medium causes localized heating. This sets in a buoyancy-driven convection flow, and a temperature gradient exists around the beam path. The resulting refractive index gradient causes a change in the beam path and intensity distribution. This coupled phenomenon involving the intensity distribution, fluid velocity and temperature describes the evolution of the beam.

The order-of-magnitude of the velocities in free convection is small and if the beam energy is not very high, the flow can be assumed to be laminar. A very powerful laser may ionize the medium and this case is not considered here. A common intensity distribution for lasers is the Gaussian distribution. Here

a Gaussian beam with the beam diameter of the order of a few millimeters is considered. The absorption coefficient of the fluid is usually small and the intensity distribution will change slowly, a significant change occurring only after a large propagation distance. The extent of thermal diffusion depends on the Prandtl Number (Pr) and is assumed to be small compared to the fluid expanse. A line source model is thus a good starting point to simulate this physical phenomenon. The evolution of light rays around a vertical line source is analyzed in *Section 2.1*. This is based on the integral method solution suggested by Vest [35]. The case of spatial extent of beam intensity is considered next and is based on the approximate solution as proposed by Lehnigk [36]. Another approximate approach using paraxial wave optics for the transient phenomenon is suggested by Kucherov [37].

2.1 Line Source Model

This is the limiting case where it is assumed that the cross section of the beam is small and tends to zero. The beam is considered to be a line heat source of equivalent power (*Figure 2.1*). The system reduces to a 2D case due to radial symmetry with respect to the buoyancy force. Under the boundary layer and Boussinesq approximations, the governing steady state equations (in cylindrical co-ordinates) for a fluid element are:

$$\frac{\partial (ru)}{\partial z} + \frac{\partial (rv)}{\partial r} = 0 , \quad (2.1.1)$$

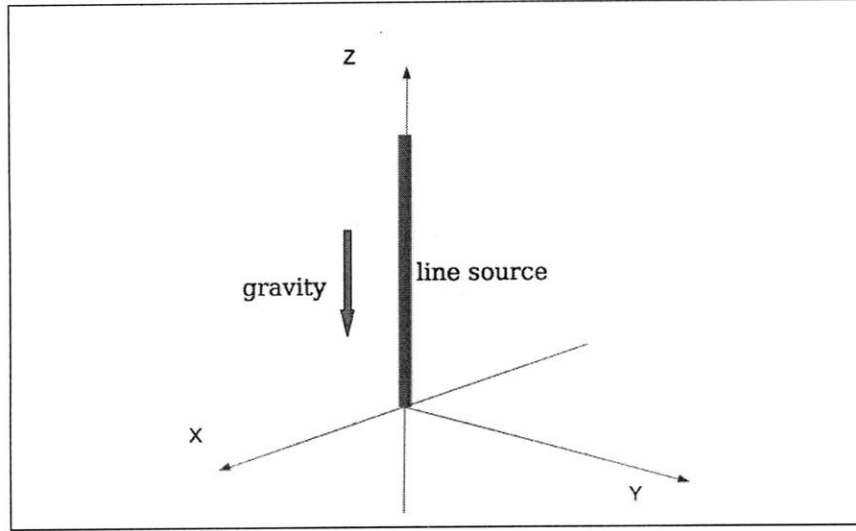


Figure 2.1: The vertical uniform line source model.

$$u \frac{\partial u}{\partial z} + v \frac{\partial u}{\partial r} = g\beta\Theta + \frac{\nu}{r} \frac{\partial}{\partial r} \left(r \frac{\partial u}{\partial r} \right) , \quad (2.1.2)$$

$$u \frac{\partial \Theta}{\partial z} + v \frac{\partial \Theta}{\partial r} = \frac{\kappa}{r} \frac{\partial}{\partial r} \left(r \frac{\partial \Theta}{\partial r} \right) . \quad (2.1.3)$$

Here u is the axial velocity along Z , v is the radial velocity and Θ is the temperature increase. The continuity equation is satisfied using a stream function ψ defined as $u = \psi_r/r$ and $v = -\psi_z/r$. Two boundary conditions on velocity arise from symmetry considerations. These are $v|_{r=0} = 0$ and $(u_r)_{r=0} = 0$. In terms of the stream function, these are equivalent to $\psi_z = 0$ and $r\psi_{rr} - \psi_r = 0$. Assuming the expanse of the fluid to be large, it then is undisturbed far away from the source. This means, as $r \rightarrow \infty$; $u = 0$, $v = 0$, $\Theta = 0$. Since the strength of the line source is constant along its length,

it is assumed that as we move near to a point on this source, all energy is released in the horizontal plane. This equates to the boundary condition $\lim_{r \rightarrow 0} (r\Theta_r) = -q'/2\pi k$.

Next, it is assumed that a similarity solution exists for this system. With a similarity parameter $\eta = Cz^q r$ the following function definitions are used: $\Theta = Az^n \theta(\eta)$ and $\psi = Bz^p f(\eta)$. Using these and the boundary conditions, the PDE reduces to the following system of ODEs.

- *Navier-Stokes equation for X direction:*

$$f''' + (f - 1) \frac{d}{d\eta} \left(\frac{1}{\eta} f' \right) - \frac{1}{2\eta} (f')^2 + \theta = 0 \quad (2.1.4)$$

- *Energy Equation:*

$$-f\theta' = \frac{1}{Pr} \frac{\partial}{\partial \eta} (\eta\theta') \quad (2.1.5)$$

- *Boundary Conditions:*

$$f(0) = 0; f'(0) = 0; \theta(0) = 0; f'(\infty) = 0; \int_0^\infty f'\theta d\eta = \frac{1}{Pr}$$

Due to the asymptotic nature of boundary conditions, a numerical solution is not possible. Instead, the integral method [35] is used to arrive at an approximate solution for $Pr = 1$. Defining $\xi = \eta/\delta$, where δ is the boundary

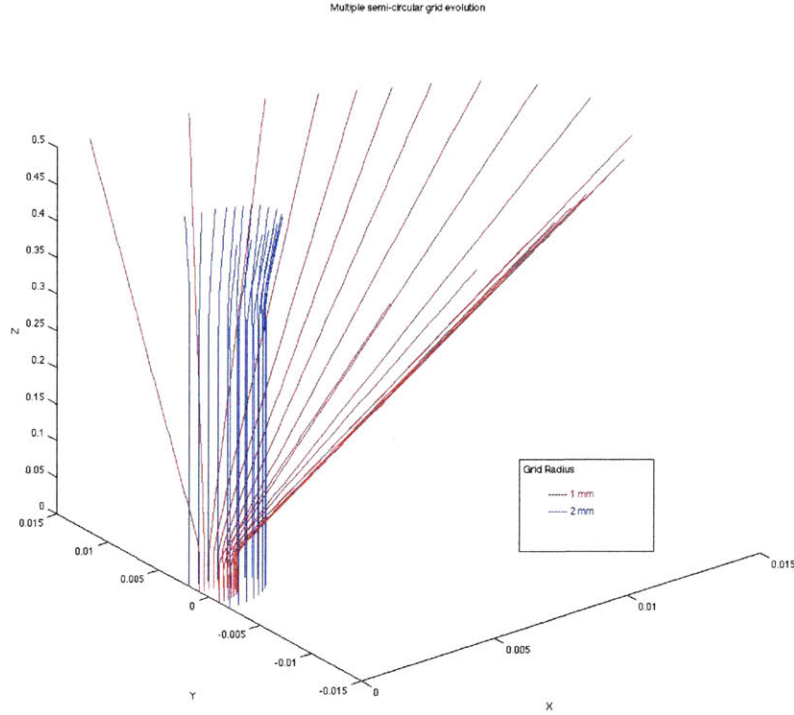


Figure 2.2: Vertical ray evolution.

layer thickness, the non-dimensional temperature is given by

$$\theta = 4.482 (\xi^2 - \xi - \ln \xi) \quad (2.1.6)$$

Using the functional definition, from this non-dimensional temperature, the spatial distribution of temperature and the resulting refractive index profile is evaluated. The evolution of a light ray in this index distribution is given by Hamiltonian equations described in *Section 1.2.2*. The evolution of two semi-circular grid of rays can be seen in *Figure 2.2*. Due to radial symmetry,

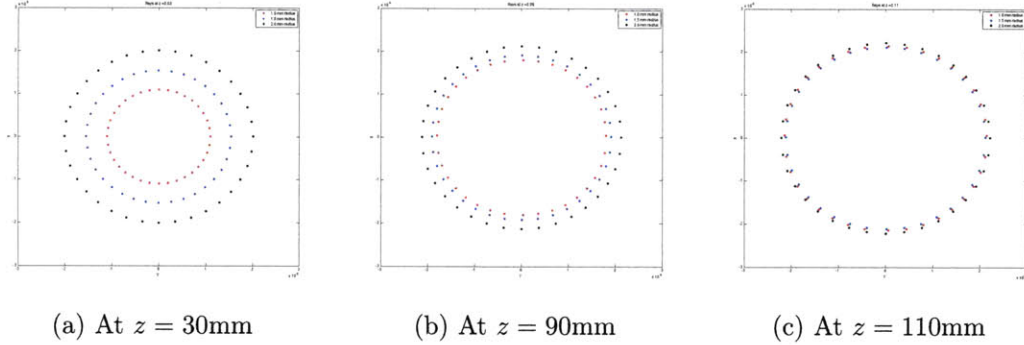


Figure 2.3: The ray pattern evolution for circular grids.

rays on the same grid deviate by same amounts. Also, since each grid sees a different index profile the two grids approach each other. This can be seen in *Figure 2.3*. Three circular grid of rays (of diameter 1 mm, 2 mm and 3 mm) entering vertically are considered. The point of intersection of each ray with a plane parallel to XY plane at different travel distances is shown. It can be seen that as the rays travel further into the medium, they approach each other signifying an increase in intensity and formation of a caustic; in this case referred to as the *thermal ring*.

2.2 Intensity as Generation Term

This model considers the intensity of the beam as a generation term in the energy equation. The solution for the temperature profile is based on the similarity solution approach suggested by Lehnigk [36] and is described below. The setup is shown in *Figure 2.4*.

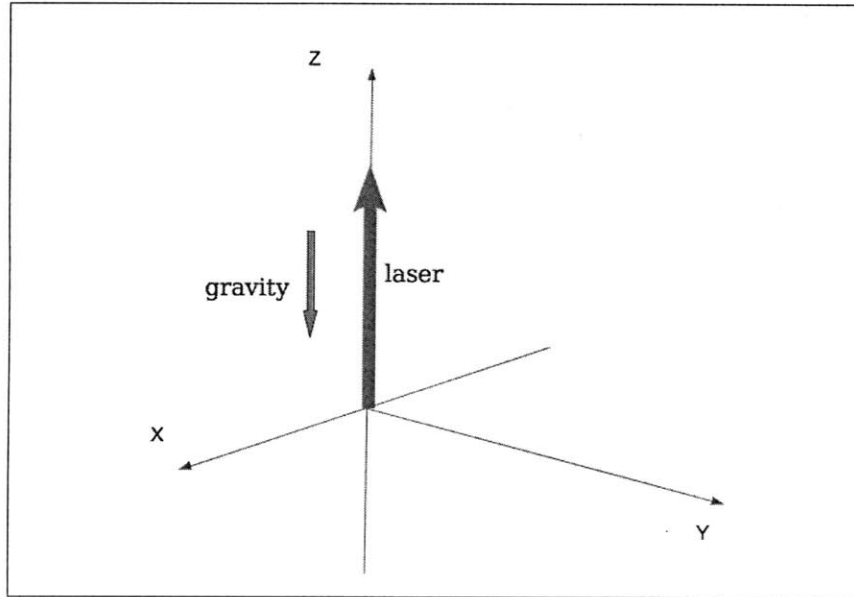


Figure 2.4: The decaying intensity model setup for vertical beam

2.2.1 Governing Equations

Because of radial symmetry, cylindrical co-ordinates are useful. Radial symmetry reduces the system to two dimensions. Using boundary layer arguments, the derivatives in the radial direction are of a greater order of magnitude than the axial gradients. Boussinesq approximation states that the density change due to localized heating is significant only in the body force term of Navier-Stokes equation. The beam when entering the fluid medium is assumed to have a Gaussian distribution, and the assumption of a slow change in intensity with propagation holds. However, there is instant dissipation of energy into the fluid, so that the beam intensity can be considered as a generation term in the energy equation. With these assumptions, the con-

tinuity, momentum and energy equations at steady state for a fluid element are

$$\frac{1}{r} \frac{\partial (rv)}{\partial r} + \frac{\partial w}{\partial z} = 0 \quad (2.2.1)$$

$$v \frac{\partial w}{\partial r} + w \frac{\partial w}{\partial z} = g\Theta + \nu \left(\frac{\partial^2 w}{\partial r^2} + \frac{1}{r} \frac{\partial w}{\partial r} \right) \quad (2.2.2)$$

$$\rho C_p \left(v \frac{\partial \Theta}{\partial r} + w \frac{\partial \Theta}{\partial z} \right) = k \left(\frac{\partial^2 \Theta}{\partial r^2} + \frac{1}{r} \frac{\partial \Theta}{\partial r} \right) + \alpha \beta I \quad (2.2.3)$$

Here, the symbols used have the following interpretation: w is Z direction velocity (vertical), v is the radial direction velocity, g is acceleration due to gravity, $\Theta (= \beta \Delta T)$ is related to excess temperature above ambient, T_∞ is ambient fluid temperature, ν is kinematic viscosity, β is thermal expansion coefficient, k is thermal conductivity of fluid, κ is thermal diffusivity of the fluid, α is absorption coefficient of the fluid for the laser beam, I is local intensity of the laser beam [W/m^2] and Pr is the Prandtl number.

A stream function ϕ is used that satisfies the continuity equation by definition. Two boundary conditions arise from symmetry of the situation. They are $v|_{r=0} = 0$, $(w_r)_{r=0} = 0$ and $(\Theta_r)_{r=0} = 0$. Another boundary condition used is that energy being convected from a plane perpendicular to the path direction is equal to the total beam power below this plane.

2.2.2 Similarity Solution

Next, a similarity solution is assumed to exist. Using a similarity parameter $\xi = r/a(z)$ the following function definitions are assumed: $\phi = \nu h(z)f(\xi)$ and $\theta = H(z)F(\xi)$. It can be shown [36] that the function definition for a, h, H, X (in terms of constant α_1) are $a = a_0 \exp(\alpha z/4)$, $h = h_0$, $H = (\alpha_1 h_0/a_0^4) \exp(-\alpha z)$ and $X = X_0 \exp(\alpha z/2)$. Substituting into *Equation 2.2.2* and *2.2.3* gives the following ODEs

$$\frac{1}{\xi} f''' - \frac{1}{\xi^2} f'' + \frac{1}{\xi^3} f' + \frac{1}{2} \alpha h_0 \frac{1}{\xi^2} (f')^2 + \frac{\alpha_1 g}{\nu^2} F = 0, \quad (2.2.4)$$

$$F'' + \frac{1}{\xi} F' - \alpha h_0 Pr \left(\frac{1}{\xi} f' F \right) + \frac{\alpha \beta}{k} \frac{a_0^6 X_0}{\alpha_1 h_0} Y = 0. \quad (2.2.5)$$

Further simplification occurs with a choice of functions $q(\xi) = \alpha h_0 f(\xi)$ and $Q(\xi) = (\alpha g \alpha_1 h_0 / \nu^2) F(\xi)$ and defining $\sigma = (\alpha^2 g \beta / \nu^2 k) a_0^6 X_0$, so that the ODEs are

$$\frac{1}{\xi} q''' - \frac{1}{\xi^2} q'' + \frac{1}{\xi^3} q' + \frac{1}{2\xi^2} (q')^2 + Q = 0, \quad (2.2.6)$$

$$Q'' + \frac{1}{\xi} Q' - Pr \frac{1}{\xi} q' Q + \sigma Y = 0. \quad (2.2.7)$$

The boundary conditions in terms of these functions are $q(0) = 0$, $q'(0) = 0$, $Q'(0) = 0$. A numerical solution is avoided in this case again, due to the asymptotic boundary conditions. Similar to the integral method, two functions that satisfy the boundary condition: $q^* = \zeta(1 - \exp(-\xi^2))$ and

$Q^* = \gamma \exp(-\xi^2)$ are assumed. These would satisfy the above ODEs for some ζ^* and γ^* which can be evaluated from the third order equation in γ - *Equation 2.2.8*. This is under the assumption $\xi \ll 1$. It can be proven that the value of γ to consider is the root closer to the origin [36].

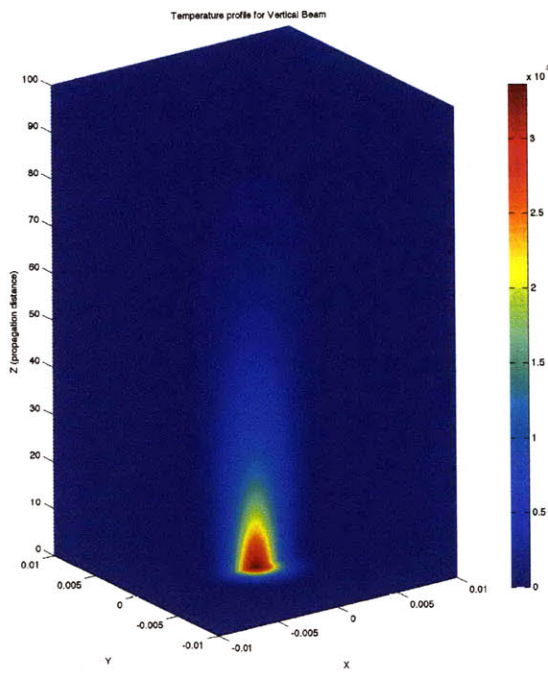
$$2Pr^2\gamma^3 - 16(2Pr - 1)\gamma^2 - 8(1 - Pr)\sigma\gamma + \sigma^2 = 0 \quad (2.2.8)$$

A further assumption of $0 < \sigma \ll 1$ leads to the reduction of the order of equation for $\gamma (= \lambda\sigma)$ and the following relation for the dimensionless temperature holds

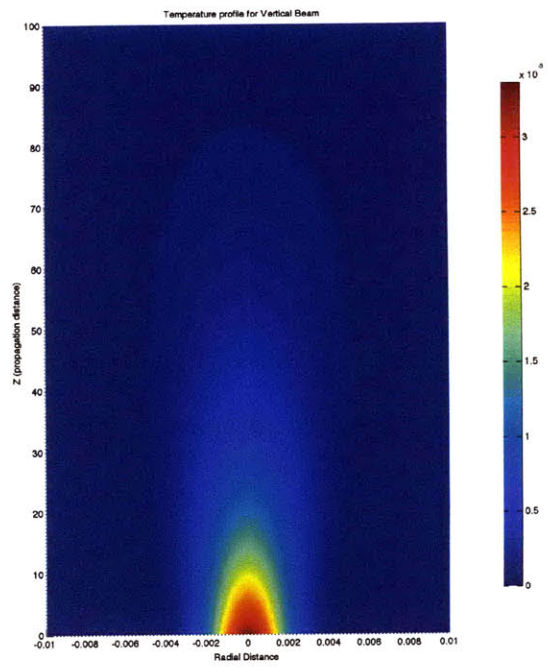
$$\Theta = \frac{\nu^2\sigma}{4\alpha g a_0^4} \exp(-\alpha z - \xi^2). \quad (2.2.9)$$

2.2.3 Refractive Index Profile

With the above nondimensional temperature, a simulation for water at 300K with the following properties $\alpha = 5 * 10^{-2}[m^{-1}]$, $\beta = 0.003317[K^{-1}]$, $\nu = 8.3334 * 10^{-7}[m^2s^{-1}]$, $k = 0.61519[Wm^{-1}K^{-1}]$, $a_0 = 0.002[m]$ and $X_0 = 0.52/(\pi a_0^2)[Wm^{-2}]$ was carried out. Using the functional definitions, the spatial temperature distribution was evaluated. This is shown in *Figure 2.5*. Once the temperature profile is available, assuming that the refractive index is a function of temperature, the refractive index profile is evaluated using the nonlinear equation for the refractive index of liquid water as a function of wavelength, temperature and pressure [38]. This is shown in *Figure 2.6*.



(a) 3D Temperature profile



(b) Temperature in XZ plane

Figure 2.5: Temperature Profile for the Vertical Beam in water at 300K

2.2.4 Ray Evolutions

The Screen Hamiltonian method can now be used to evaluate the path of a ray through this index profile. Three circular grids of rays of diameter 1 mm, 2 mm and 3 mm at the entry plane are considered. They are assumed to enter the medium at $z = 0$ and with ray momentum components $p_x = 0, p_y = 0$. As the refractive index goes on decreasing with increasing radius, the rays bend outwards. The points where these rays intersect a plane along the propagation direction (and parallel to XY plane) are evaluated. The ray positions at such planes are shown in *Figure 2.7* for increasing z distance. Due to the radial symmetry the deviation for rays initially on the same grid should be same. This is verified by the simulated results. Again, a thermal ring is seen to emerge as in *Figure 2.3*.

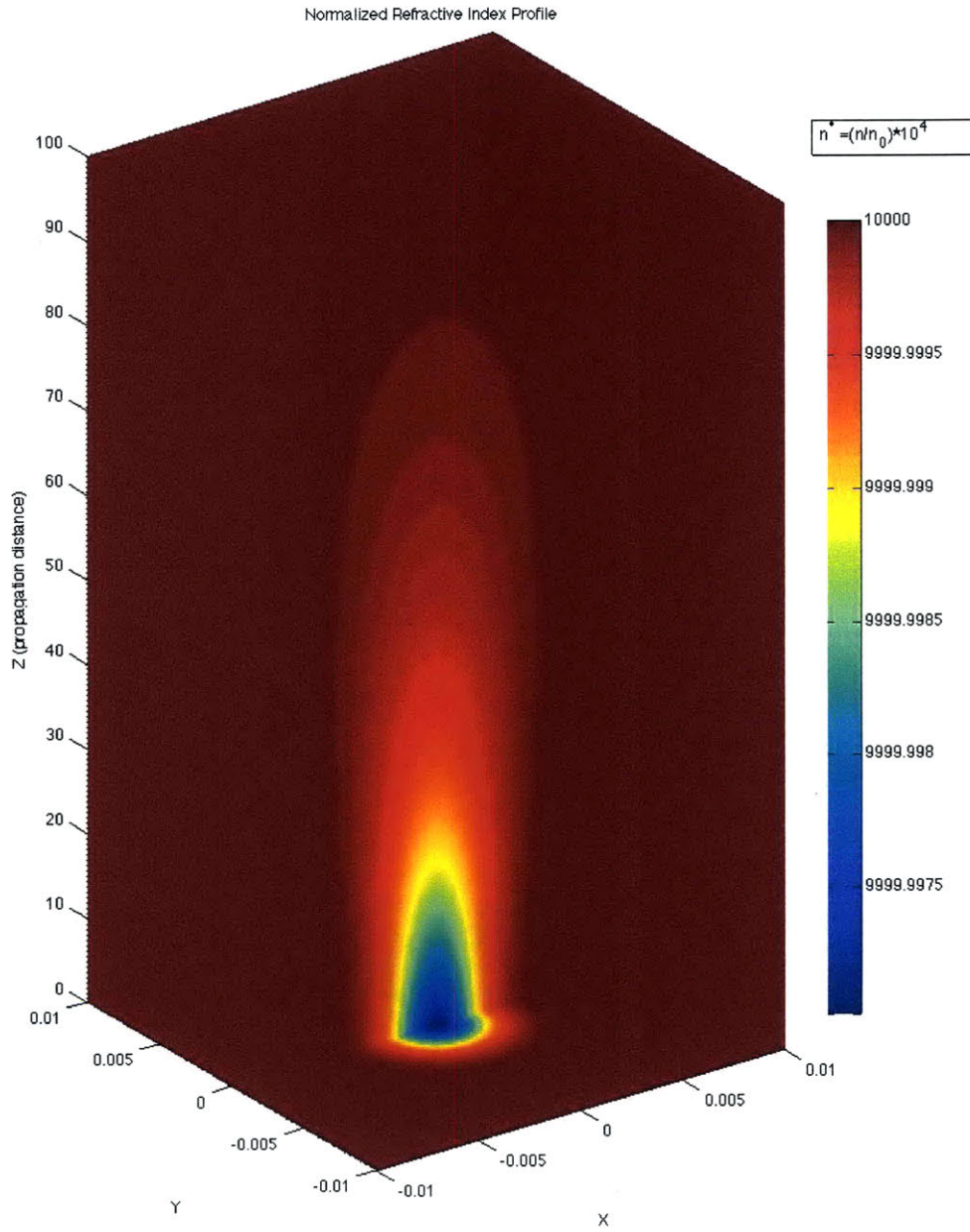
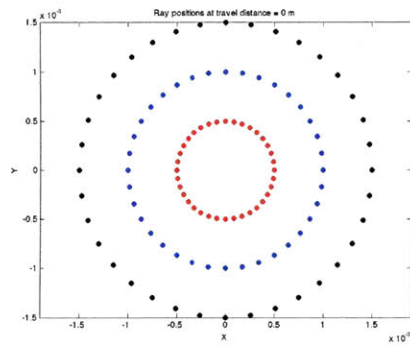
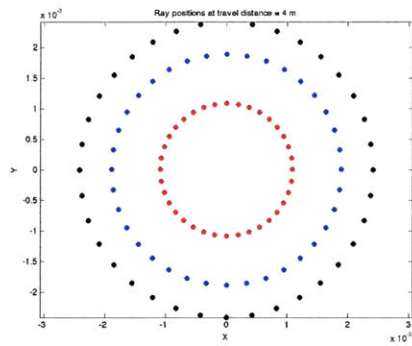


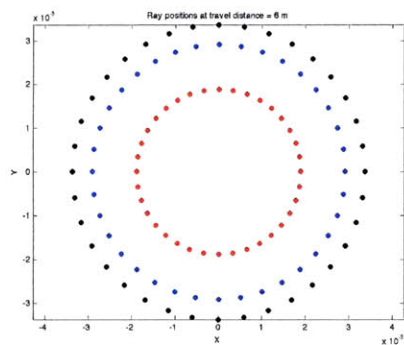
Figure 2.6: Normalized Refractive Index Profile. $\{n^* = (n/n_0) \times 10^4\}$



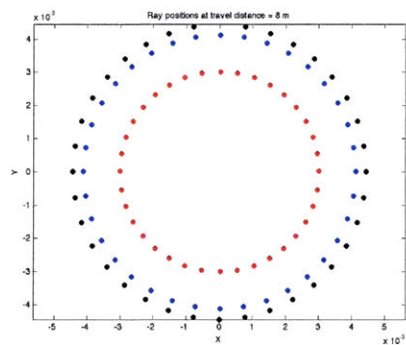
(a) At $z = 0\text{m}$



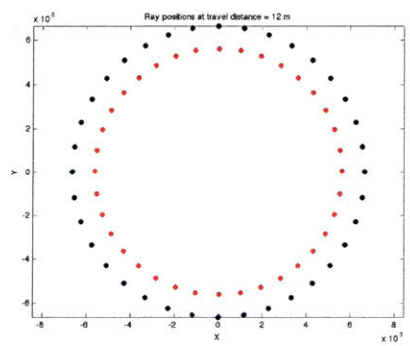
(b) At $z = 4\text{m}$



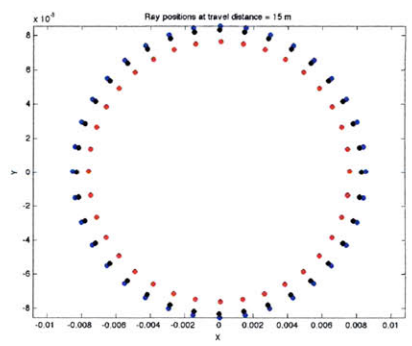
(c) At $z = 6\text{m}$



(d) At $z = 8\text{m}$



(e) At $z = 12\text{m}$



(f) At $z = 15\text{m}$

Figure 2.7: The ray pattern evolution for a vertical beam.

Chapter 3

Horizontal Laser Beam

A laser beam entering the fluid medium in a direction perpendicular to the gravity force is considered in this chapter. The fluid is locally heated due to energy dissipation from the laser by absorption. The convection field in combination with gravity in this case causes a radially non-symmetric temperature profile which creates a refractive index gradient. The path and intensity distribution of the beam is thus expected to change with propagation. The steady state evolution of a horizontally traveling laser beam is evaluated.

As in the case of a vertical laser beam, a line source model would be a good starting point since the characteristic radius of a laser is usually small and a significant change in intensity distribution is expected to occur only over a large distance. However, the horizontal case is more involved than the

vertical one as there is no radial symmetry that could simplify the attempt of an analytic solution. *Section 3.2* discusses this case where the laser beam is replaced by an equivalent linear source whose strength is constant through the propagation distance. The case of a decaying line source is considered in *Section 3.3*.

3.1 Laser Propagation in a Cross-flow

The introduction of high power lasers has brought forth a focus on the coupling effect between the electric fields present and the medium through which the laser propagates [1-4]. The distortion created by the travel through a medium is usually compensated by assuming the existence of an equivalent focusing/defocusing lens [6, 39]. Hence the term - *thermal lens*. The thermal lensing has been experimentally observed and there have been attempts of theoretical explanation of the phenomena. An elaborate mathematical treatment is given by Livingston [1] for the case of a high intensity Gaussian beam traveling through air.

Under the approximations of geometrical optics, the coupling of heat dissipation in the medium for a cross-wind perpendicular to the beam propagation is considered by Livingston. Starting from the Eikonal equation [17] and the conservation of photon flux along the propagation direction, a first order perturbation analysis is applied. The initial distribution of the laser is assumed Gaussian and there is a constant flow of the medium in the positive

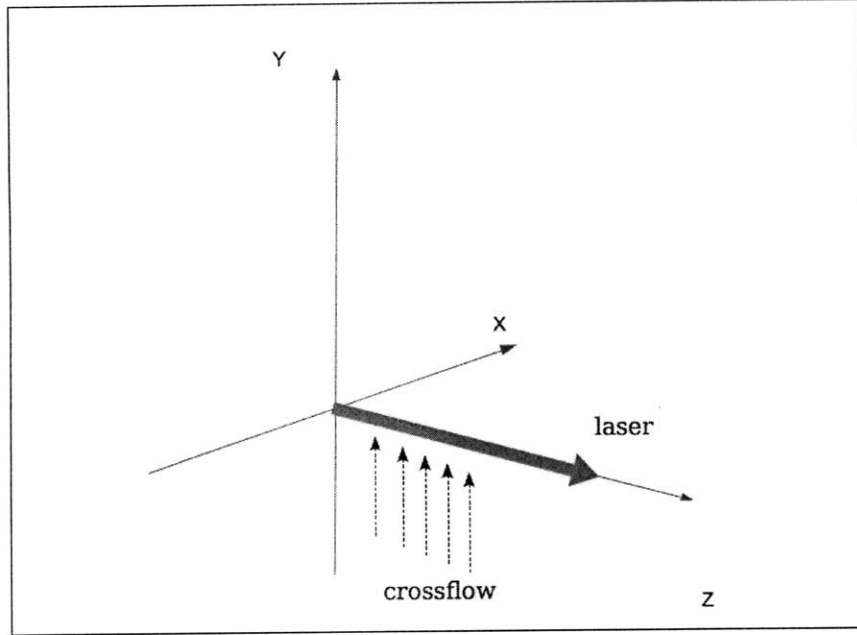


Figure 3.1: The Livingston model for natural convection.

Y direction.

Extension to free convection for water

The theory is developed for air as the propagation medium, and it is easily extended to water (*Appendix A*). It is suggested in [1] that considering the case of natural convection to be a 90° rotation of the cross-flow case is reasonable. On these lines, for the setup shown in *Figure 3.1*, the intensity at any co-ordinate z along the optical axis is given by:

$$\frac{I}{I_0} = \exp \left\{ -p_1 - K e^{-(x/d_0)^2} \left[\frac{2y}{\sqrt{\pi}d_0} e^{-(y/d_0)^2} - \left(\frac{2x^2}{d_0^2} - 1 \right) \left(1 + \operatorname{erf} \left(\frac{y}{d_0} \right) \right) \right] \right\}$$

Here, d_0 - characteristic beam radius, α - absorption coefficient for the fluid, $p_1 = -\alpha z - \frac{x^2+y^2}{d_0^2}$, I_0 - the maximum beam intensity at entry and $K = -\frac{\sqrt{\pi}\beta}{\alpha d_0^2} \left(z - \frac{1-e^{-\alpha z}}{\alpha} \right)$ where $\beta = -\frac{\alpha d_0 I_0}{\rho C_p V} \left(\frac{dn}{dT} \right)$ with ρ - density, C_p - specific heat capacity and dn/dT - temperature coefficient of refractive index. The intensity propagation for a laser beam moving through water is shown in *Figure 3.2*. It can be seen that as the beam moves into the fluid, there is a shift in the location of the highest intensity spot. Initially, with a Gaussian distribution, the highest intensity is at the origin; and with increasing distance, two bright intensity spots shifted in the direction of fluid flow emerge.

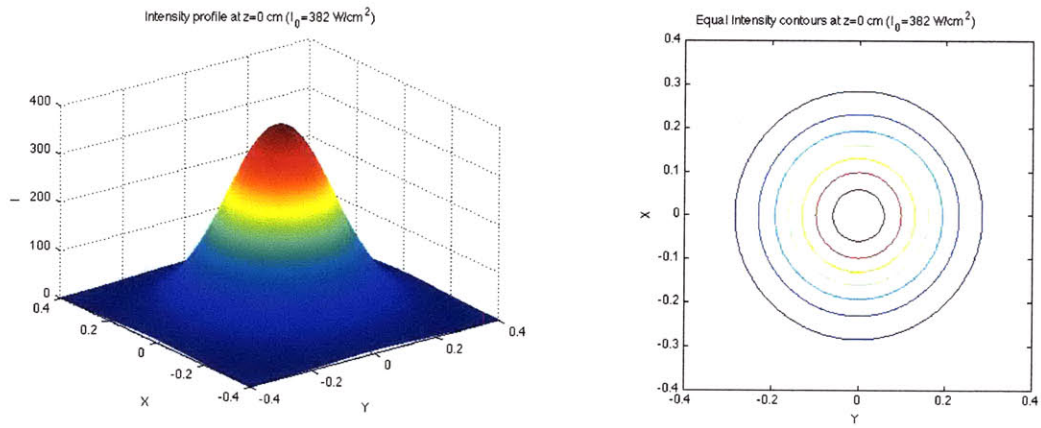
Equivalently, the propagation of a ray can be calculated as follows. In the perturbation procedure, the dimensionless refractive index change Q_0 is given by equation (25) [1] as

$$\begin{aligned} Q_0 &= \exp(-v^2 - d_0\alpha q) \cdot \int_{-\infty}^u \exp(-t^2) dt \\ &= \frac{\sqrt{\pi}}{2} \exp(-v^2 - d_0\alpha q) \cdot (1 + \operatorname{erf}(u)) \end{aligned} \quad (3.1.1)$$

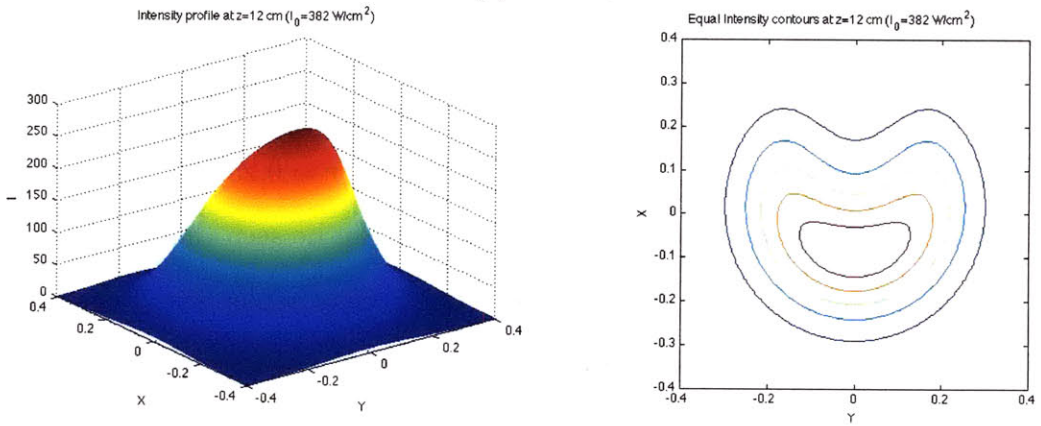
where u, v, q are the reduced spatial co-ordinates. These being equal to $x/d_0, y/d_0$ and z/d_0 respectively. The XY projection of the propagation direction, as per the definitions used, is given by \mathbf{w} and

$$\mathbf{w} = \mathbf{w}_0 + \beta \mathbf{w}_1 \quad (3.1.2)$$

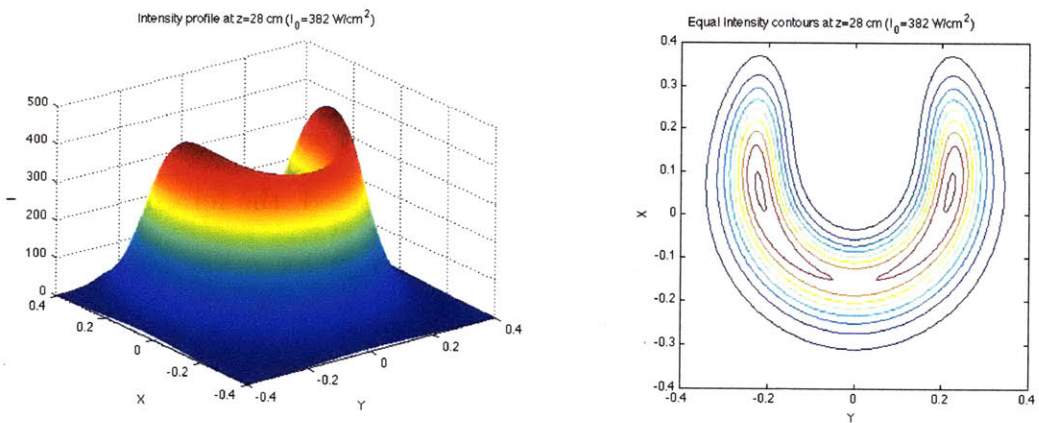
where \mathbf{w}_0 is the initial direction of a ray entry, β is the parameter defined



(a) At $z = 0\text{m}$



(b) At $z = 0.12\text{m}$



(c) At $z = 0.28\text{m}$

Figure 3.2: Intensity profile and corresponding isocontour lines along beam propagation axis.

above and \mathbf{w}_1 is given by

$$\frac{\partial \mathbf{w}_1}{\partial q} = -\nabla_{\perp} Q_0 = -\frac{\partial Q_0}{\partial u} \hat{\mathbf{x}} - \frac{\partial Q_0}{\partial v} \hat{\mathbf{y}} \quad (3.1.3)$$

Here $\hat{\mathbf{x}}$ and $\hat{\mathbf{y}}$ are the unit vectors in x and y direction. Using *Equation 3.1.1* gives

$$\mathbf{w} = \mathbf{w}_0 + \frac{\beta}{\alpha d_0} (1 - e^{-\alpha z}) \left[-e^{\left(-\frac{x^2+y^2}{d_0^2}\right)} \hat{\mathbf{x}} + \frac{\sqrt{\pi}y}{d_0} e^{-\frac{y^2}{d_0^2}} \left(1 + \operatorname{erf}\left(\frac{x}{d_0}\right)\right) \hat{\mathbf{y}} \right] \quad (3.1.4)$$

Using *Equation 3.1.4* the ray path is calculated for rays along circular grids. A sample evaluation for rays on circular grids of radii $r = 0.25\text{cm}, 0.30\text{cm}, 0.35\text{cm}, 0.40\text{cm}$ and 0.45cm is shown in *Figure 3.3*. It can be seen that as the beam propagates into the medium, the rays initially on a circular grid do not propagate in the same manner. Also, there is a densing of rays at two locations above the origin which is in the same direction as the cross flow and signifies redistribution of the intensity distribution.

The above treatment is consistent with the assumption that the free convection case is the same as a rotated forced convection case. In [1], in order to describe the accuracy of the phenomena observed, the forced convection solution was matched to the closed form solution for a line source. This was assuming that for air Pr is close to $5/9$ for which the closed form solution is available [41]. However, the next sections approach ray evolution for a generic fluid by evaluating the spatial refractive index profile for natural

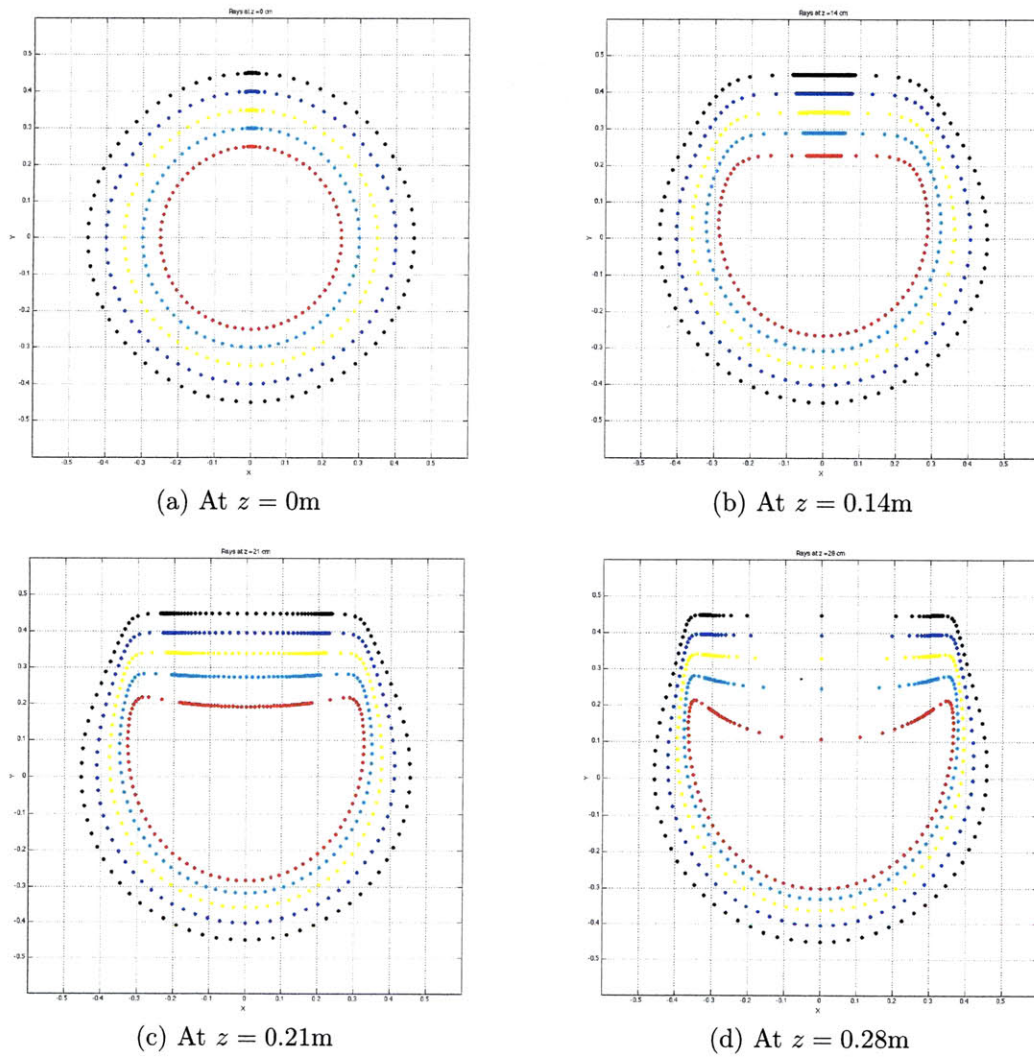


Figure 3.3: Ray Pattern at different propagation distance for forced convection

convection. Here too, the laser beam is considered to be a linear heat source with equivalent heat flux input into the fluid.

3.2 Uniform Line Source

The model consists of a line source of energy positioned horizontally in an undisturbed fluid medium of large expanse. The gravity force is in a direction perpendicular to the plane containing the line source. This is similar to the case of a constant heat flux from a thin horizontal wire in a quiescent medium. The strength of the source is assumed to be such that the convection flow that sets in is in the laminar regime. The natural convection plume arising from a linear heat source has been explored in an approximate manner [40-54]. The similarity solution approach is used to determine the velocity and temperature profile. The numerical treatment by Fujii [43] suggests one such method of analysis that is found to match well with the experimental results [46, 47] and will be the basis of the analysis here.

3.2.1 Governing Equations

As mentioned above, the line source strength creates a laminar natural convection field. Since the strength of the source is constant along its length, the flow is assumed planar (XY plane), as shown in *Figure 3.4-b*, and hence the temperature profile is identical in planes perpendicular along the length.

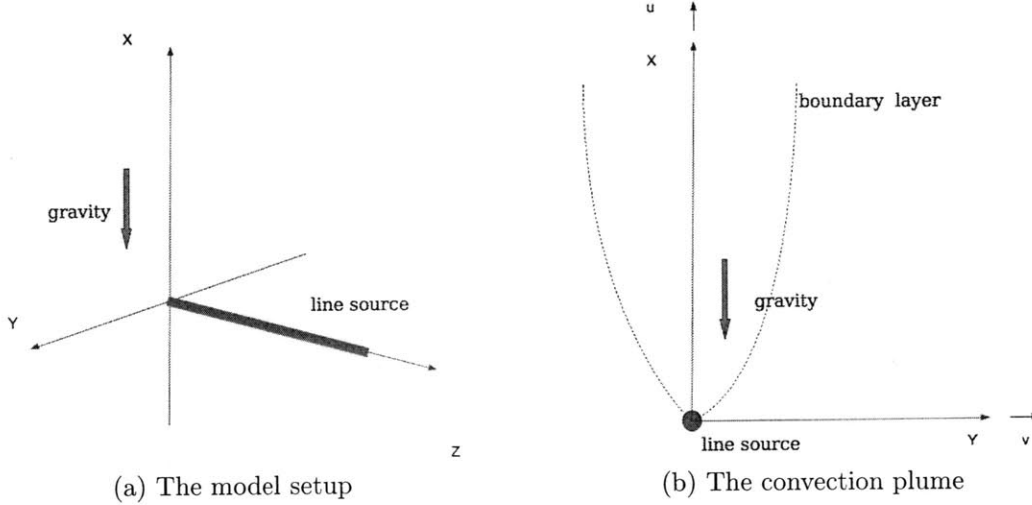


Figure 3.4: The uniform horizontal line source model

The fluid that comes in contact with the heat source expands and the density gradients cause it to move upwards forming a plume which is similar to a boundary layer. Using the *Boussinesq approximation* as before, we assume that the density change is significant only in the force term. Under these approximations; the continuity, momentum and energy conservation equations for a fluid element are:

$$\frac{\partial u}{\partial x} + \frac{\partial v}{\partial y} = 0 , \quad (3.2.1)$$

$$u \frac{\partial u}{\partial x} + v \frac{\partial u}{\partial y} = g\theta + \nu \frac{\partial^2 u}{\partial y^2} , \quad (3.2.2)$$

$$u \frac{\partial \theta}{\partial x} + v \frac{\partial \theta}{\partial y} = \alpha \frac{\partial^2 \theta}{\partial y^2} . \quad (3.2.3)$$

Here, the x and y direction velocities are u and v respectively. The other symbols used are g - acceleration due to gravity, ν - kinematic viscosity, α -

thermal diffusivity, T - temperature at a point, T_∞ - the ambient temperature, β - thermal expansion coefficient, Pr - Prandtl number, and the excess temperature is defined as $\theta = \beta\Delta T = \beta(T - T_\infty)$.

The boundary conditions by symmetry are $v|_{y=0} = 0, u_y|_{y=0} = 0, \theta_y|_{y=0} = 0$. By assuming that the fluid is undisturbed from its initial state far away from the source the boundary conditions become, $u|_{y=\infty} = \theta|_{y=\infty} = 0$.

3.2.2 Similarity Solution

It can be seen that the system of governing equations is coupled. The approach to simplify this is to assume a similarity solution and convert the PDEs to ODEs which can be solved subject to the boundary conditions. On these lines, the following function definitions are assumed: Similarity parameter $\xi = y/a(x)$, stream function $\psi = \nu h(x)f(\xi)$ and $\theta = H(x)F(\xi)$. The continuity equation is satisfied by this definition of stream function. Using these, the momentum and energy equations reduce to:

$$f''' + (ha' - h'a)(f')^2 + h'a(ff'') + \left(\frac{ga^3H}{\nu^2h}\right)F = 0 \quad (3.2.4)$$

$$F'' - Pr\left(\frac{ahH'}{H}\right)f'F + Pr(ah')fF' = 0 \quad (3.2.5)$$

Here a, h, H are functions of x only and the *prime* ($'$) notation for these are derivatives with respect to x , whereas for F and θ the derivatives are with respect to ξ (*Appendix B*). For these to be ODEs in ξ , the coefficients should

be independent of x . The choice of a, h, H may not thus be unique. Two such definition pairs are suggested by Gebhart [47] and Fujii [43]. The relations suggested in the latter are used as these match with the experimental results better [46]. The exponent of x in these definitions comes about by dimensional analysis and the requirement that the coefficients in the equations be constants [45]. The correct choice is:

$$a(x) = \left(\frac{\nu^2}{g\beta\theta_l} \right)^{1/5} x^{2/5}$$

$$h(x) = \left(\frac{g\beta\theta_l}{\nu^2} \right)^{1/5} x^{3/5}$$

$$H(x) = \beta\theta_l \left(\frac{g\beta\theta_l}{\nu^2} \right)^{-1/5} x^{-3/5}$$

Here, θ_l is a constant dependent on the rate of heat transfer from the source. With these definitions, $(ha' - h'a) = -1/5$, $h'a = 3/5$, $\frac{ga^3H}{\nu^2h} = 1$, $\frac{ahH'}{H} = -3/5$ and the governing equations form the following coupled ODEs

$$f''' + \frac{3}{5}ff'' - \frac{1}{5}f'^2 + F = 0, \quad (3.2.6)$$

$$F'' + \frac{3}{5}Pr(fF)' = 0. \quad (3.2.7)$$

The boundary conditions for these functions are

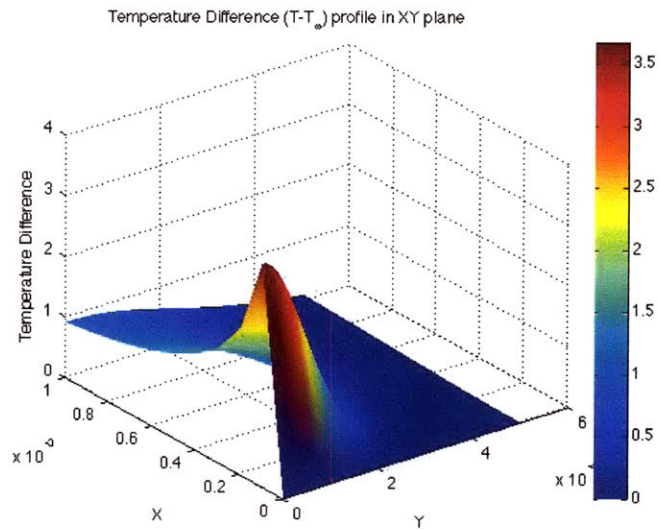
$$\begin{aligned} \xi = 0; \quad f = 0, \quad f' = 0, \quad f'' = 0, \quad F' = 0, \\ \xi = \infty; \quad f' = 0, \quad F = 0. \end{aligned} \quad (3.2.8)$$

This boundary value problem is converted to an initial value problem (by assuming values for $F(0)$ and $f'(0)$) and solved by the Runge-Kutta method to give the dimensionless temperature. This is then converted to the spatial temperature profile by the function definition. *Figure 3.5* shows the temperature excess in the XY plane.

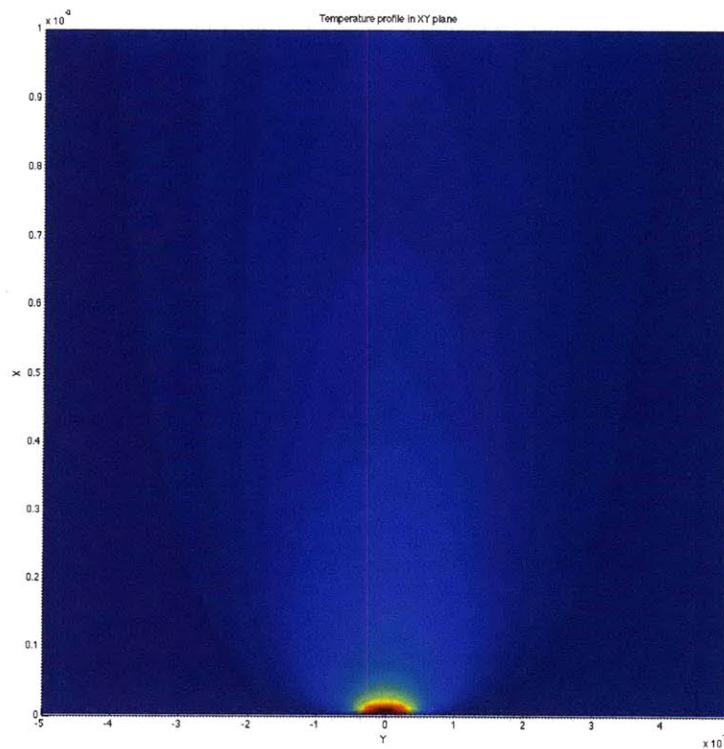
3.2.3 Ray Evolution

Once the temperature profile is available, the corresponding refractive index profile is easily obtained. This is shown in *Figure 3.6*. With the assumption of a uniform line source, this is the refractive index profile in any plane perpendicular to the source along the propagation direction.

The Hamiltonian equations are now evaluated for a ray propagation in such an index distribution. A circular grid of rays is considered to see the effect of such an index field. These are rays at 1° separation and a radius of 1mm. A finer separation of 0.05° is considered in the range $89^\circ < \theta < 91^\circ$ to better understand the phenomena. The pattern of point of intersection of these rays with XY planes along the propagation is shown in *Figure 3.7*. With increasing travel distance, the circular distribution of rays is changed with the rays initially within the $70^\circ - 110^\circ$ region moving outward. A characteristic *flattened top* shape is seen to form. Although this is not true *flattening* as the enclosed area is clearly greater than at the start.

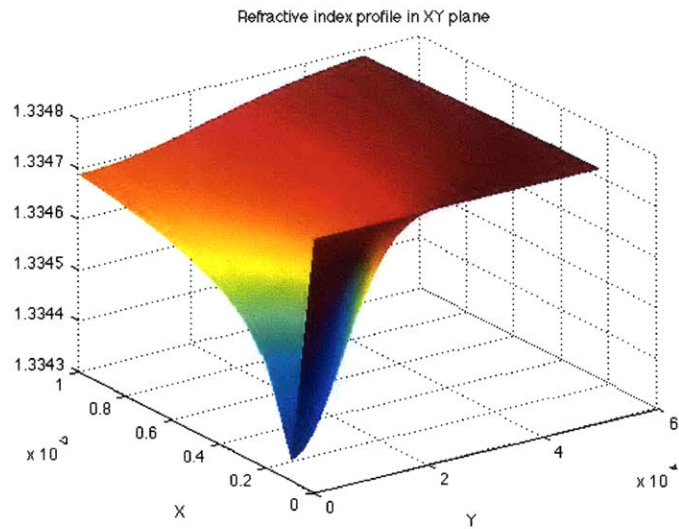


(a) Temperature cut-plot (first quadrant)

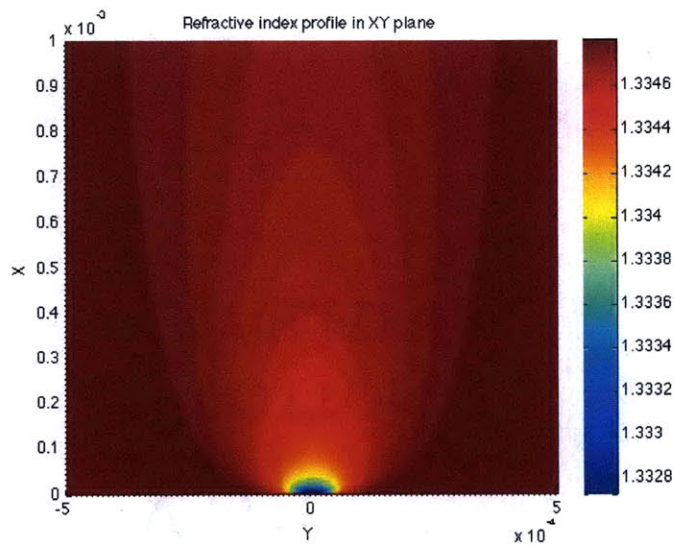


(b) Temperature excess (XY) plane

Figure 3.5: Temperature excess ($T - T_{\infty}$) in the XY plane for a uniform horizontal line source.



(a) Refractive Index cut-plot (first quadrant)



(b) Refractive Index (XY) plane

Figure 3.6: Refractive Index in the XY plane for a uniform horizontal line source.

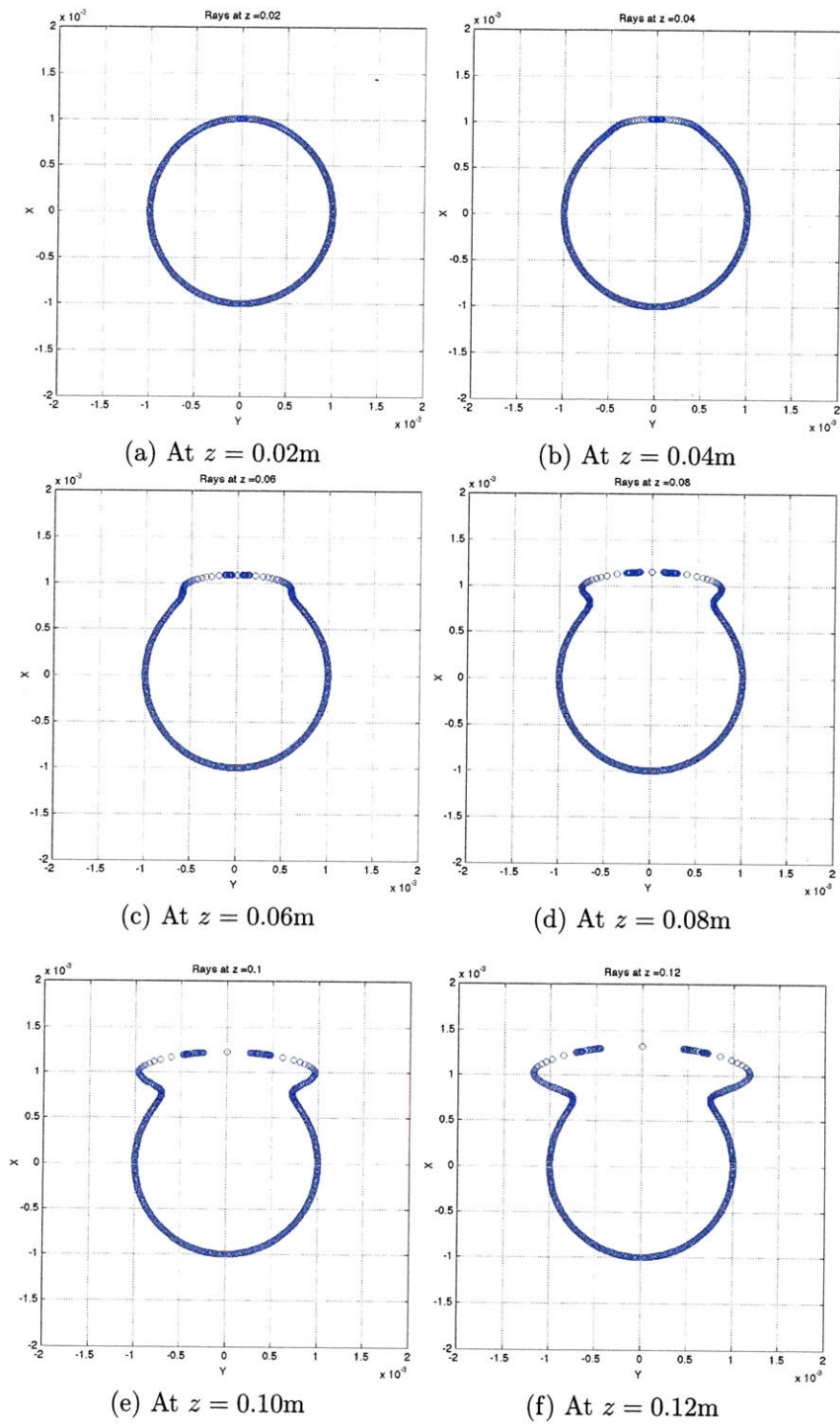


Figure 3.7: Ray pattern for a 0.001m circular grid.

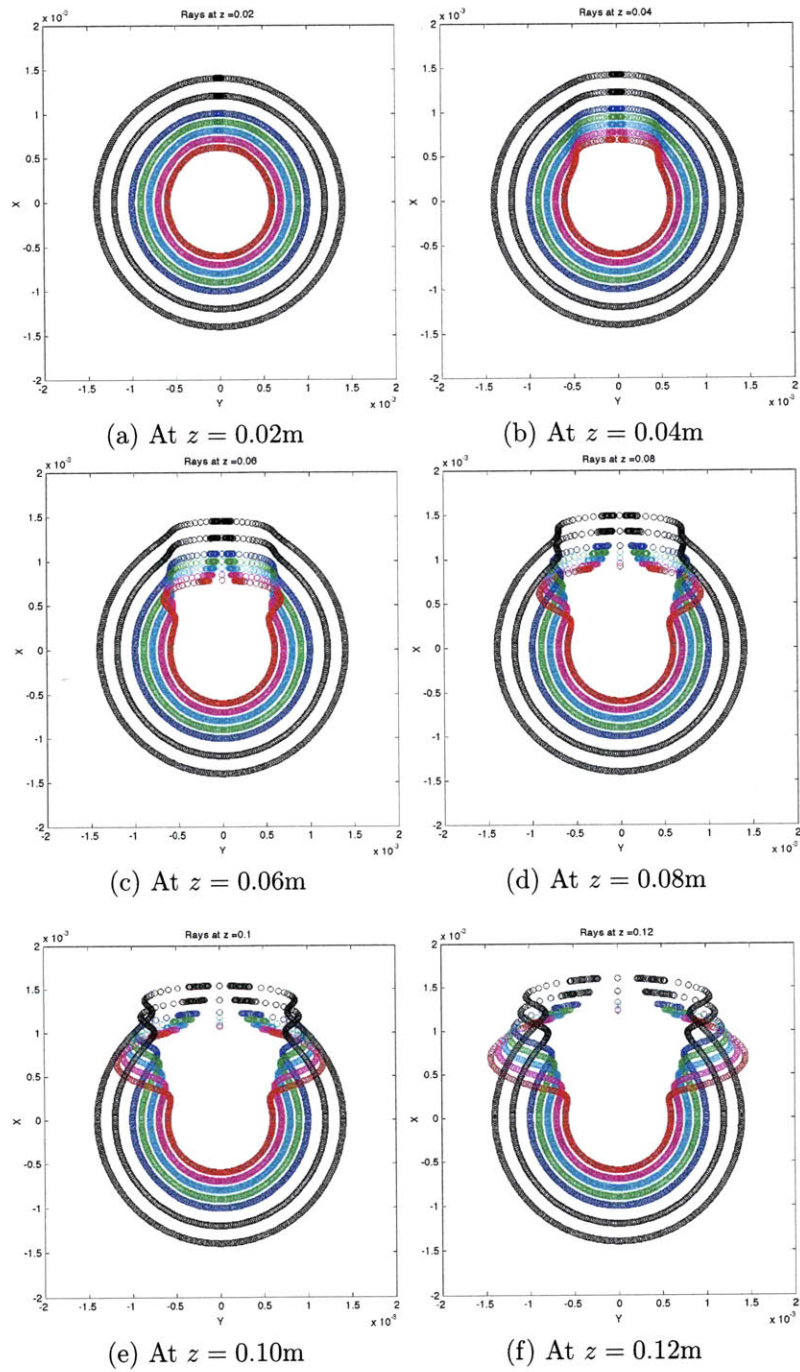


Figure 3.8: Ray pattern for multiple circular grids ($r = 0.6\text{mm}$, 0.7mm , 0.8mm , 1.0mm , 1.2mm and 1.4mm).

The outward movement of the rays is more pronounced for rays on a circular grid closer to the source (located at origin and into the plane of the paper in the figures). This can be seen in *Figure 3.8* where seven circular grids of different radii are considered. Circular grids with same sampling of rays at radii of 0.6mm, 0.7mm, 0.8mm, 0.9mm, 1.0mm, 1.2mm and 1.4mm enter the medium with their momentum vector along the z axis. The ray pattern at different planes is calculated as earlier. The distribution of rays changes with propagation and there is noticeable densing of rays and caustic formation at two locations (*Figure 3.8-d*). This is equivalent to saying that an intensity redistribution takes place for a beam propagating in the fluid medium with the formation of two high intensity spots. The behavior is similar to the intensity evolution (solved analytically) for a laser beam in a cross flow (*Section 3.1*).

3.3 Decaying Line Source

The previous section considered the laser beam to be replaced by an equivalent linear source whose strength is constant along the beam travel. This is reasonable to assume provided that the absorptivity of the fluid medium is small and the intensity is slow varying. In a medium with appreciable absorption, to first order approximation, the intensity variation along beam travel is exponential. Here, as the power pumped into the fluid decreases along propagation, the fluid motion is expected to be a 3D phenomenon.

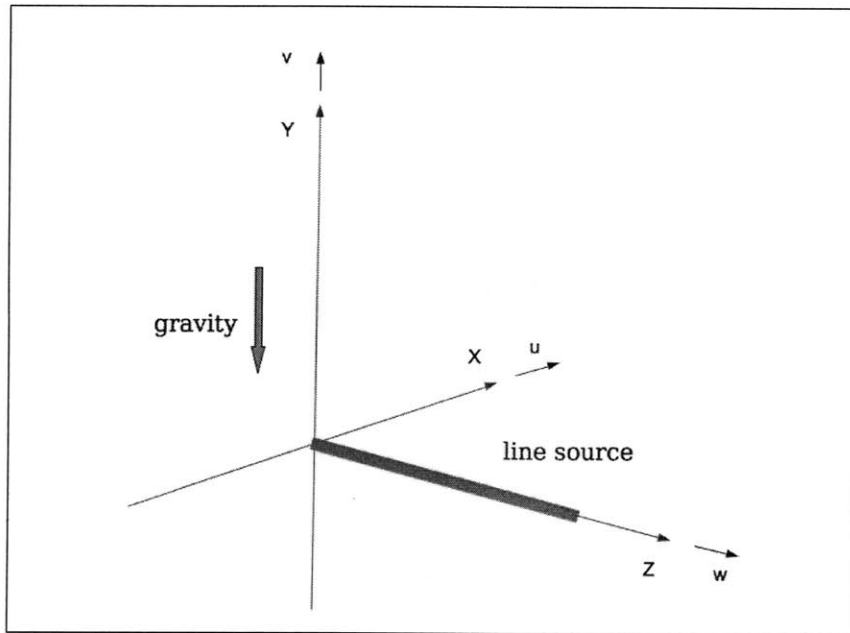


Figure 3.9: The decaying line source model.

This has been visualized in thermal lensing experiments. In accordance, a simplified model is to consider the laser beam to be a *decaying line source* with the source strength decreasing along the direction of propagation.

A similarity solution for a decaying line source was proposed by Boyd [55]. The natural convection field was assumed to be in the laminar regime and the region of interest is located far away from the source at origin. The governing equations are simplified under boundary layer formulation and assuming that the Boussinesq approximation applies. The assumptions made are incompressibility of the fluid, negligible motion pressure gradient and no viscous dissipation [56, 57]. A qualitative estimation of ray behavior in the region where this similarity solution is valid is explored in what follows.

The governing boundary layer equations for a horizontally propagating laser beam (gravity forces perpendicular to the plane containing the beam) in an initially undisturbed medium under the set of assumptions stated are:

$$\frac{\partial u}{\partial x} + \frac{\partial v}{\partial y} + \frac{\partial w}{\partial z} = 0 , \quad (3.3.1)$$

$$u \frac{\partial v}{\partial x} + v \frac{\partial v}{\partial y} + w \frac{\partial v}{\partial z} = \nu \frac{\partial^2 v}{\partial x^2} + g\beta T , \quad (3.3.2)$$

$$u \frac{\partial w}{\partial x} + v \frac{\partial w}{\partial y} + w \frac{\partial w}{\partial z} = \nu \frac{\partial^2 w}{\partial x^2} , \quad (3.3.3)$$

$$u \frac{\partial T}{\partial x} + v \frac{\partial T}{\partial y} + w \frac{\partial T}{\partial z} = \kappa \frac{\partial^2 T}{\partial x^2} . \quad (3.3.4)$$

Here u, v, w are the velocities in x, y, z directions respectively, T is the temperature increase above ambient, ν is kinematic viscosity, g is acceleration due to gravity, β is thermal expansivity of the fluid and κ is the fluid thermal diffusivity. *Equation 3.3.1* is the mass continuity equation, *Equations 3.3.2, 3.3.3* are the Navier-Stokes equations for y and z directions respectively, and *Equation 3.3.4* is the energy conservation equation for a fluid element at steady state. Boundary conditions follow from symmetry and the consideration that the fluid is undisturbed far away from the source.

As in earlier cases, to convert these partial differential equations to a system of ordinary differential equations a set of similarity definitions are used [55]. The boundary value problem is then converted to an initial value problem and a numerical computation of the ODEs can be attempted. This is dif-

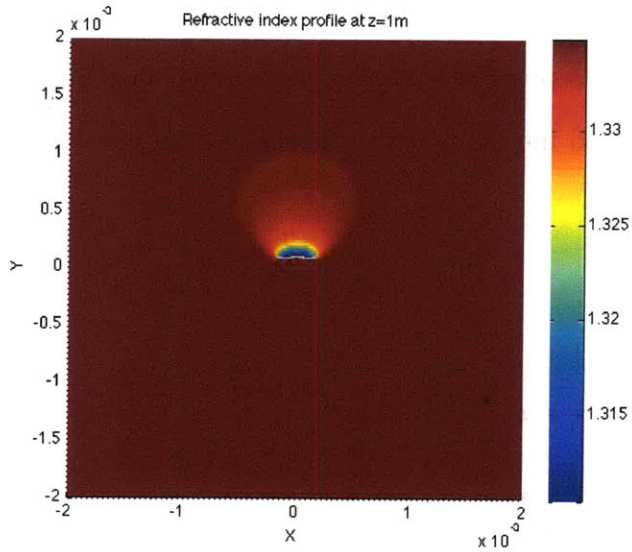


Figure 3.10: Refractive Index (XY) profile for the decaying line source at $z = 1\text{m}$.

difficult due to additional unknown parameters (treated as eigenvalues for the problem) introduced by the similarity definitions. Hence, the integral formulation is used to approximate the temperature profile. Polynomial functions that satisfy the boundary conditions are assumed and the unknowns in their definitions are evaluated subject to minimization of a chosen residual function. This gives the spatial temperature profile and the resulting refractive index profile. *Figure 3.10* shows the steady state refractive index profile in a plane parallel to XY and located at a distance of 1m along the propagation distance for a laser beam of maximum power $P_0 = 0.12\text{W}$ travelling through undisturbed water at 27°C .

The Screen Hamiltonian method can now be used to determine the behaviour

of rays through this index distribution. A circular grid of rays entering horizontally into the fluid is considered and the ray paths for a few rays are shown in *Figure 3.11*. The condition for the validity of the similarity solution requires $Gr_y \gg 1$, which is satisfied by only the rays on the circular grid of radius $\gtrsim 8\text{mm}$; and hence only rays on a grid of radius greater than this value of 8mm are considered. The pattern of the intersection of rays with planes parallel to XY at different distances along propagation gives an idea of the redistribution of the rays and hence the intensity. This is evaluated for three circular grids of radii $r = 8\text{mm}, 9\text{mm}$ and 10mm entering horizontally into the fluid and shown in *Figure 3.12*. The initially circular grid again deforms into a flat top shape structure similar to the earlier cases. The inner grid deformation is more pronounced than the outer ones and this causes a densing of rays at two locations above the origin (again in the direction of fluid motion) signifying that the intensity at these spots is higher. However, these are peripheral rays and provide only a qualitative indication of ray behavior in a convective field generated by the horizontal decaying line source.

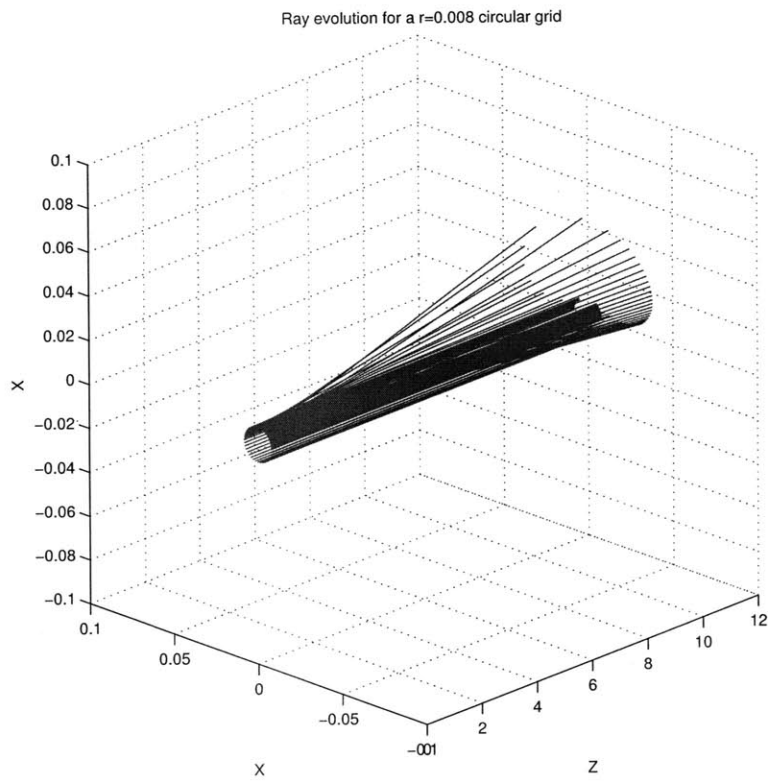
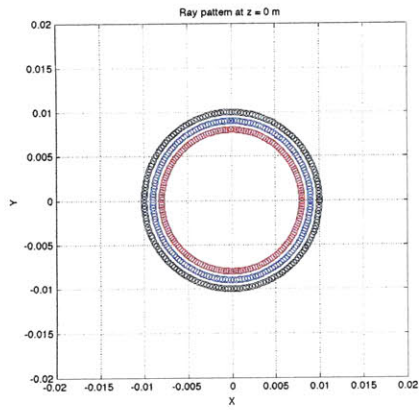
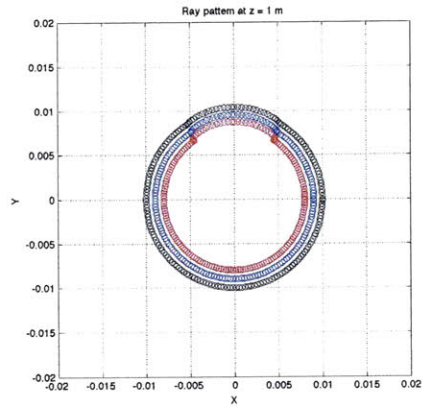


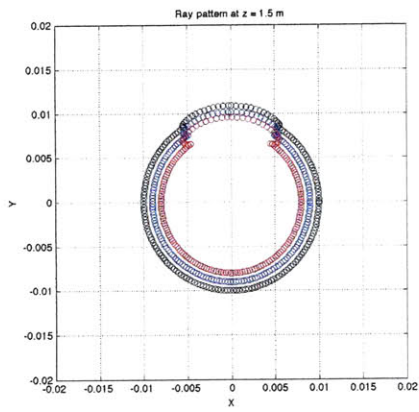
Figure 3.11: Ray evolution for a $r = 8\text{mm}$ circular grid (decaying line source).



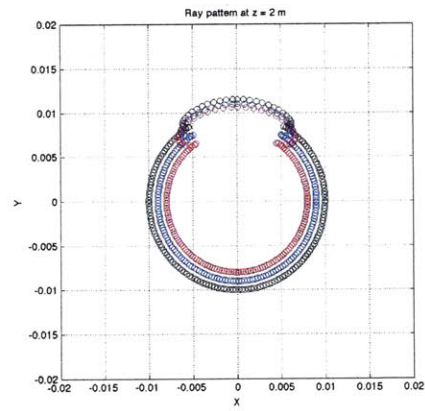
(a) At $z = 0\text{m}$



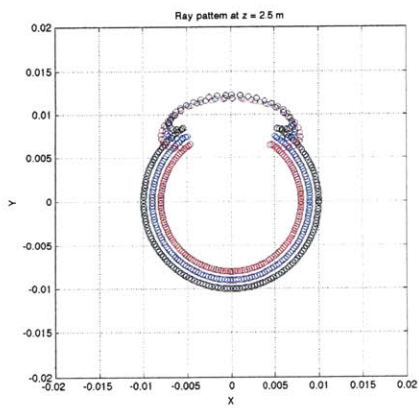
(b) At $z = 1.0\text{m}$



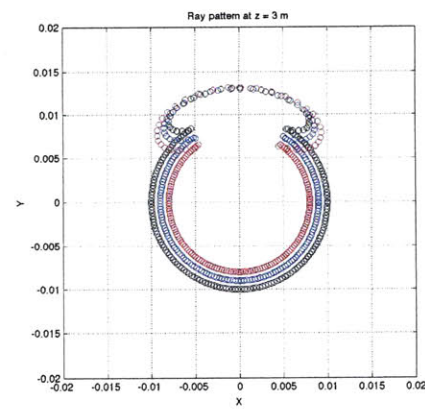
(c) At $z = 1.5\text{m}$



(d) At $z = 2.0\text{m}$



(e) At $z = 2.5\text{m}$



(f) At $z = 3.0\text{m}$

Figure 3.12: Ray pattern for multiple circular grids ($r = 8\text{mm}, 9\text{mm}, 10\text{mm}$).

Chapter 4

Interferometric Visualization

As the analysis shows, the change in temperature and refractive index due to the convection induced by laser energy is not high. Interferometry is thus a good candidate for visualizing the heating effect due to its sensitivity at measuring small phase changes. The effect of a refractive index gradient build up in the medium through which a laser beam propagates due to its energy is called *Thermal Lensing*. There have been different models that approximate the behaviour of the medium to be a thin lens [6, 58]. An experimental technique that is used to measure the nonlinear property of a thermal lens is the Z-scan technique. Here the change in intensity of a probe laser due to the heating by a pump laser is measured at an aperture placed in the far-field [59, 60]. This however requires the propagation model for the beam (which is being analyzed in the first place). Another technique that has been used to accurately visualize refractive index gradients is Interferometry [62-65].

In this thesis, the spatial temperature distribution in a steady state convection field has been experimentally estimated by measuring the phase changes with a Mach-Zehnder interferometer. The interferograms are analyzed using both, the Fourier techniques and the Phase Shifting Method (PSM).

4.1 Experimental Setup

The optical setup for visualizing thermal lensing consists of the Mach-Zehnder interferometer at its core and is shown in *Figure 4.1*. A He-Ne laser source (2mW @543nm, Newport™) is used as the probe beam to visualize the refractive index change. A collimated beam is produced using a spatial filter (SF) and a lens (L) combination. A Newport™ Three-axis Spatial Filter fitted with a *M60X* microscope objective and a $5\mu\text{m}$ diameter pinhole is used with a plano-convex lens of focal length 125mm. Using a spatial filter enables obtaining a larger beam size to visualize the area of interest. The collimated beam enters the Mach-Zehnder interferometer at beam splitter BS1 and is divided into two. One beam follows the reference path along BS1-M1-BS2 and the other follows the test path BS1-M2-BS2. Here M1 and M2 are plane mirrors supported on kinematic mounts that can rotate the mirrors along all the 3 co-ordinate axes. The mirror M1 is connected to a piezo stage (single axis $20\mu\text{m}$ piezo NanoFlex Stage, ThorLabs™) operated by a controller (single channel benchtop piezo controller, ThorLabs™). This enables changing the position of M1 along BS1-M1. A sample containing the fluid is introduced

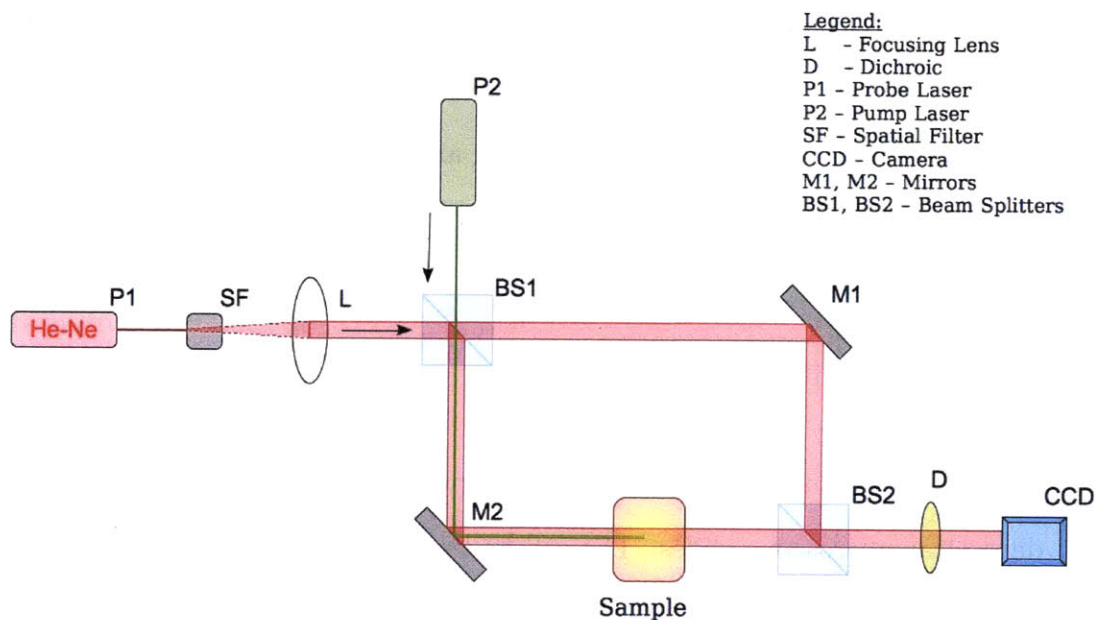


Figure 4.1: The Experimental Setup.

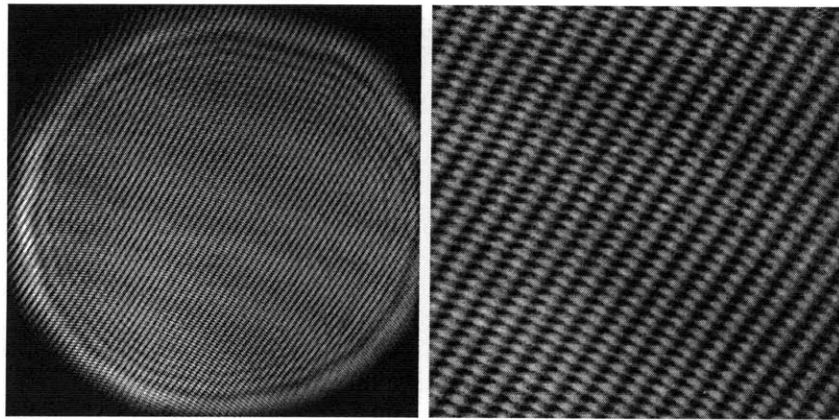
in the test path. A high power laser beam - the pump beam - from a diode laser (120mW @660nm, Power Technology Incorporated™) passes through the sample in the same direction as the probe beam generating a thermal lens and creating a refractive index profile. The two probe beams recombine at beam splitter BS2 to produce the interference pattern which is captured by the CCD (Model A504K, Basler™). A dichroic (D) helps blocking out the high intensity pump beam and thus avoiding saturation of the camera pixels. For a strong thermal lensing the liquid sample should have a high dn/dT and a low specific heat and thermal conductivity [66]. Hence pure water and alcohols may not be the best solvents to visualize. Therefore the samples chosen are aqueous solution of dyes that are absorbing at the pump beam

wavelength. With the red pump beam, two ideal choices are Malachite Green (maximum absorption at 616.5nm) [67] and Toluidine Blue (absorption band 560 + nm) [68]. Experimental observation and analysis are shown for Toluidine Blue in the following sections.

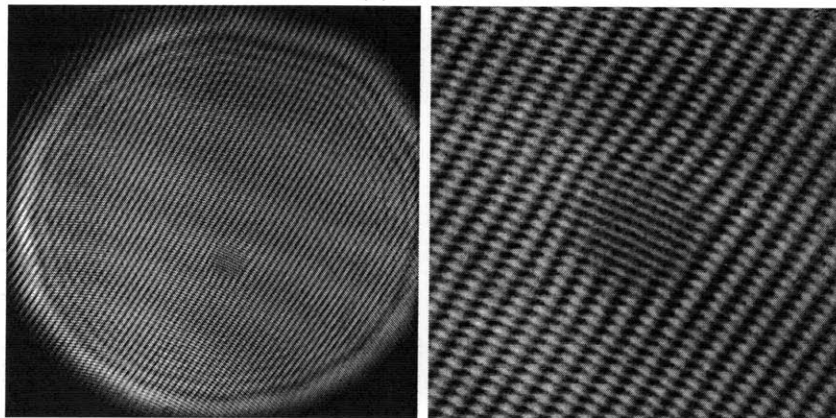
4.2 Observations

The aqueous solution of Toluidine Blue dye was held in a cell made from standard clear microscope slides. The cell had a path length $l_{sample} = 22.38\text{mm}$ and a liquid cross section of $25.15\text{mm} \times 63.18\text{mm}$. The liquid free surface was open to ambient air and the setup was isolated from environmental vibrations by floating the optical table. The distance that the pump beam travels within the sample was chosen such that there is not much attenuation of the beam intensity. This was done to closely resemble the case of a uniform source along the path length. The transient phenomenon was captured on the CCD camera at 400 frames per second. A few frames of the entire interferogram and the area near the pump beam is shown in *Figure 4.2*.

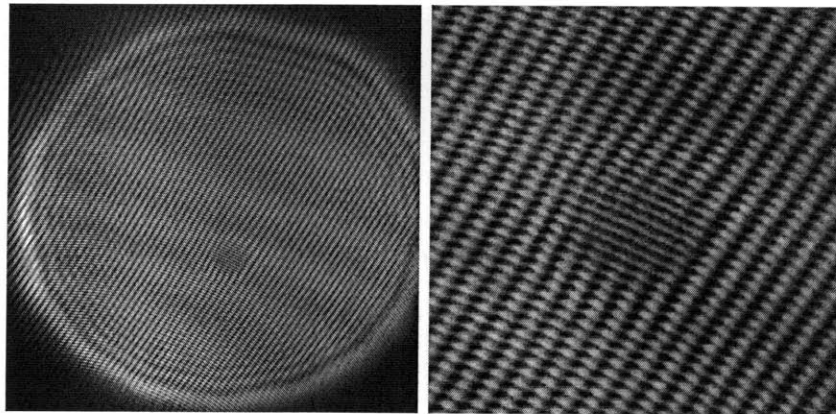
In order to use the Fourier method for interferogram analysis, a carrier (spatial) frequency is introduced by tilting one of the mirrors. This is evident in the fringe pattern visible in frame 0. It can be seen that due to the change in refractive index profile, there is a gradual shift of the fringe pattern near the beam. Also, frame 700 onwards, there isn't much change in the fringe pattern indicating that a steady state is reached.



(a) Frame 0



(b) Frame 75



(c) Frame 700

Figure 4.2: Interferograms (entire pixel area on the left and area near the beam on the right) for a Toluidine Blue sample heated by a 120mW beam.

Next, for the PSM, interferograms with phase shifts were recorded. As indicated in *Section 1.4.2.2* four interferograms with a gradual phase shift of $\pi/4$ are needed. This is achieved by moving the mirror M1 along BS1-M1 in increments of $\lambda_p/4$ with the piezo controller, λ_p being the wavelength of the probe beam. To ensure the alignment of the reference arm, it is necessary to calibrate the piezo movement. The idea behind the process is that a path change of λ_p should leave the interferogram unchanged as the phase would then change by 2π . Hence interferograms were captured by moving the mirror by distances around the probe wavelength and comparing it with the initial interferogram (\mathcal{I}_0). Given the errors due to wind disturbances, external vibrations (if any, after floating the table) etc., the distance at which the interferogram was most similar to \mathcal{I}_0 is taken to be λ_p . The piezo movement and camera capture were synchronized with LabVIEW™ and MATLAB™.

4.3 Interferogram Analysis

The Fourier method as stated in *Section 1.4.2.1* is used to isolate the phase information from the interferogram. Due to the carrier frequency introduced by tilting one of the mirrors, the frequency domain will have three distinct bright spots including the central bright spot as shown in *Figure 4.3*. The two off-axis spots contain the phase information. The spot in the +ve half plane is shifted to the origin and an inverse Fourier transform gives the phase. The image before the pump beam is turned on gives the phase difference ϕ_0

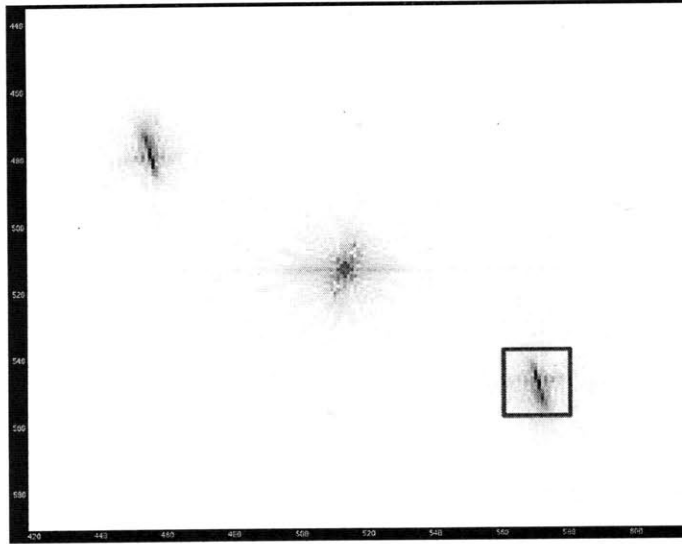


Figure 4.3: The interferogram in Fourier domain with one side spot highlighted.

between the two arms of the interferometer. Once, the pump beam enters the sample and creates the thermal lens, the steady state interferogram gives the phase difference ϕ_1 . The inverse Fourier transform gives a wrapped phase due to the arctangent function used. The unwrapping procedure suggested by Takeda [26] is used to get the correct phase. This is shown in *Figure 4.4*. The difference $\Delta\phi = \phi_1 - \phi_0$ gives the phase difference caused just due to heating.

This method gives the phase change along the entire path length of the sample. The assumption of uniform beam strength throughout the sample means the index profile has no gradient along the beam direction. Thus the

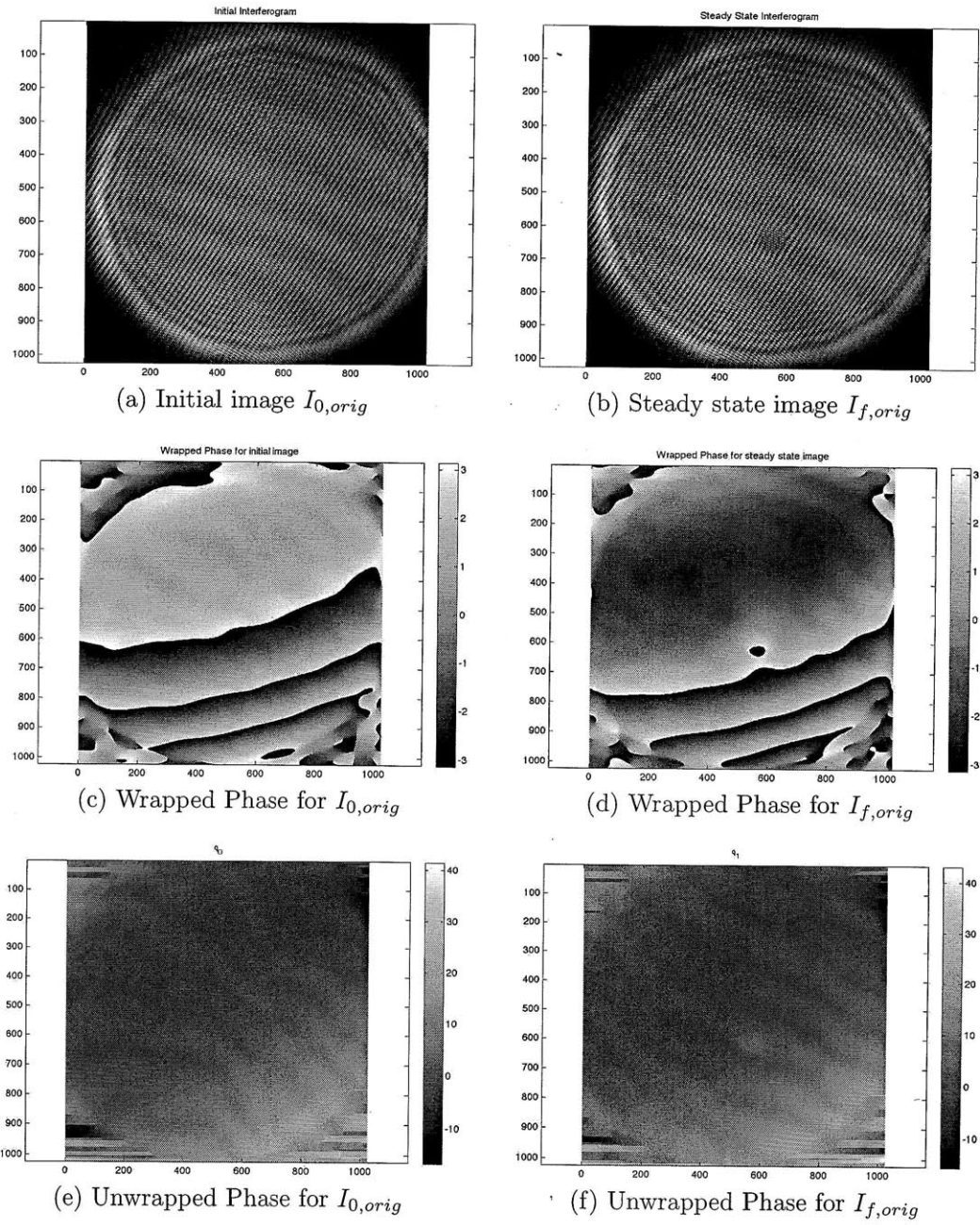


Figure 4.4: The Fourier method for interferogram analysis.

change in refractive index is given by

$$\Delta n = n(x, y, t) - n_0 = \left(\frac{\Delta\phi}{2\pi l_{sample}} \right) \lambda_p \quad (4.3.1)$$

where n_0 is the initial refractive index (at ambient conditions). The transient phenomenon showing the change in refractive index after the pump beam enters the Toluidine Blue sample is shown in *Figure 4.5*. As can be seen in subfigure *a*, the disturbance is more or less symmetric around the beam. This signifies that the mode of heat dissipation at this point is conduction. With time, the disturbance spreads asymmetrically and the formation of a convection plume is evident. The system reaches a steady state quickly and there is no significant change in refractive index thereafter.

A beam centre is defined to be the location of highest temperature (and hence lowest refractive index) at steady state, and the vertical line through this centre is defined the centre-line. The evolution of the change in refractive index along this centre-line gives a better idea about the transient process. Noting that the camera pixel size is $12\mu\text{m}$ and converting it to spatial coordinates (m), this evolution with time is shown in *Figure 4.6*. As can be seen here, the change in refractive index at time $t = 0.25\text{s}$ is symmetric around the beam centre. Hence the primary mode of heat dissipation is conduction at this point. The hotter fluid then moves upwards due to density gradients and the colder fluid located far away from the beam moves in towards the hotter area, and heat dissipation through convection is setup. Due to the hot fluid

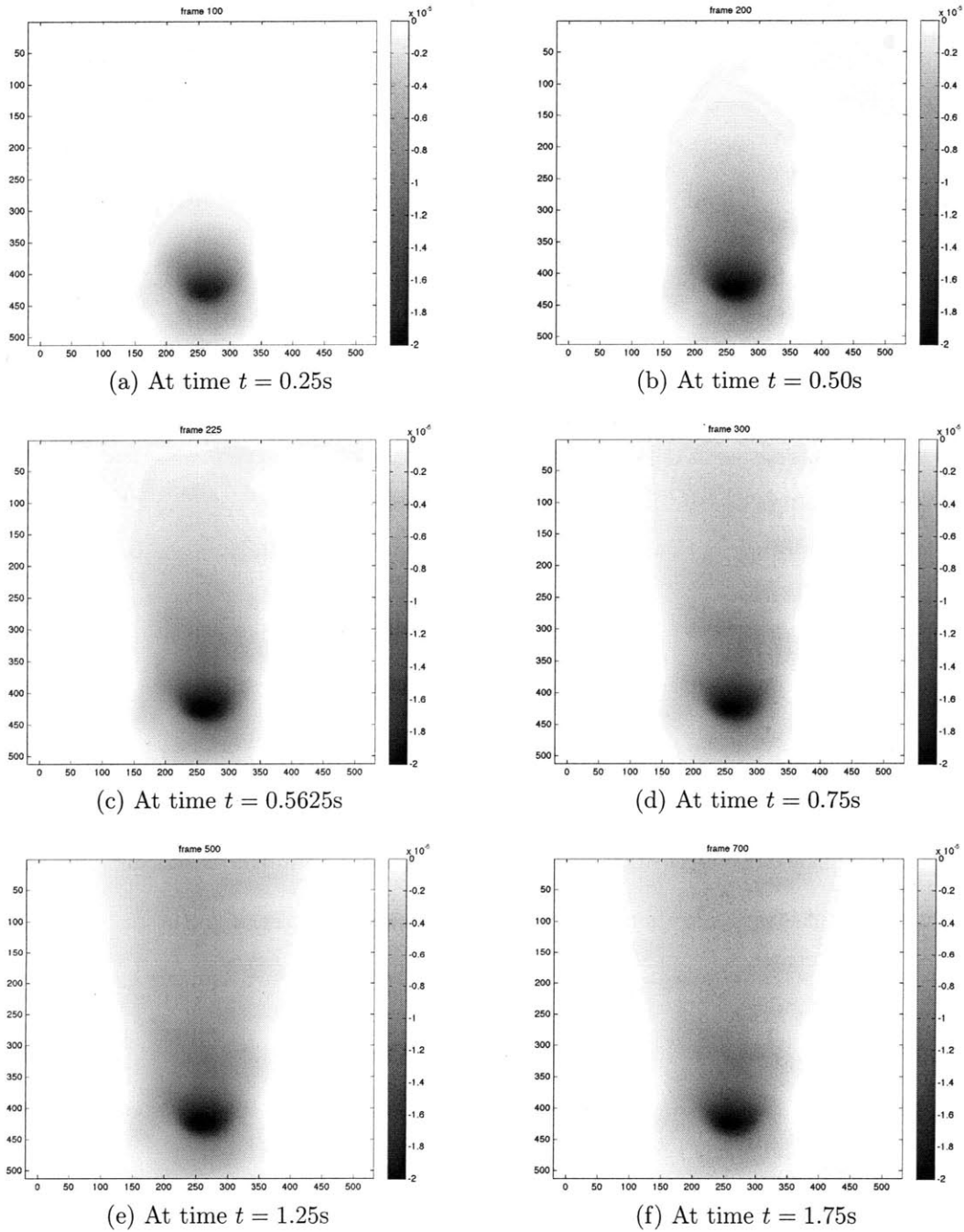


Figure 4.5: Evolution of the change in refractive index with time.

movement upwards, the index profile on the centre-line becomes asymmetric. The system then reaches a steady state with the surroundings. *Figure 4.7* shows the centre-line change in refractive index when the pump beam has just entered the sample (subfigure *a*) in comparison to the change at steady state (subfigure *b*). Note that the change in refractive index immediately after the beam entry ($t = 0.1225\text{s}$) is higher than at steady state ($t = 1.75\text{s}$). A possible reason for this is that just as the pump beam enters the sample, there is instant absorption of the beam energy by the fluid and this raises the temperature (decreases refractive index). As the beam intensity profile is symmetric, the change in refractive index around the beam centre is also symmetric. The mechanism of heat dissipation starts thereafter, first by conduction and then by convection. While the mode of heat dissipation is primarily conduction, the change in refractive index around the beam centre is still symmetric. As convection starts to dominate, the profile becomes asymmetric as explained above.

The discontinuity at the edges of the interferogram may give rise to ripples in the Fourier space causing errors in the phase recovery. This is usually corrected either by extrapolating the fringe data [31] or weighting the image data with an intensity window [26, 30, 33]. The *Hanning* and *Blackmann-Harris* windows are applied to the interferograms here. Phase retrieval by Fourier method using these windows is shown in comparison to the original image in *Figure 4.8*. Here, the sub-images *b, c, d* show the region near the pump beam (as indicated by the red box in sub-image *a*).

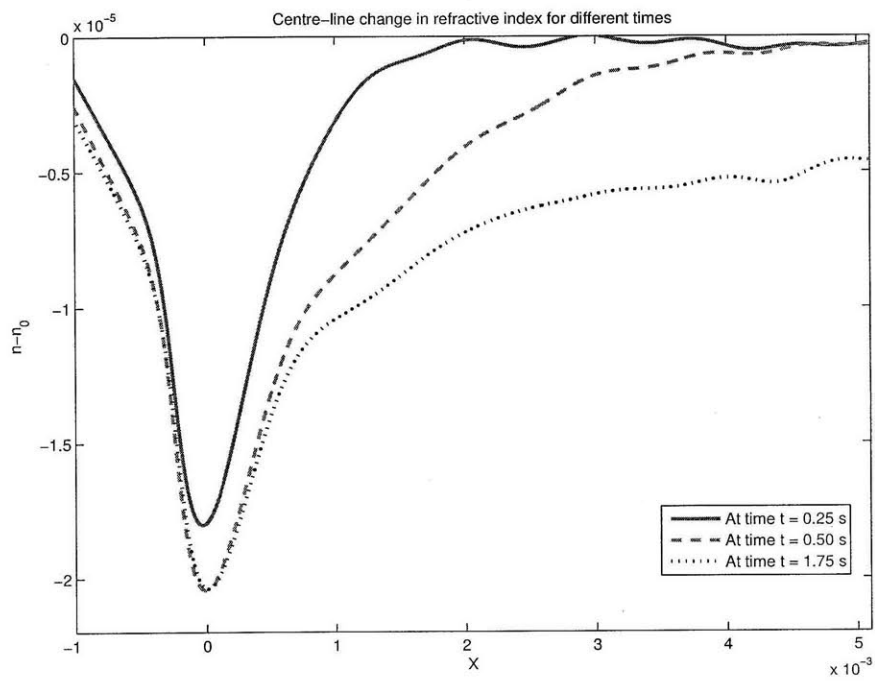
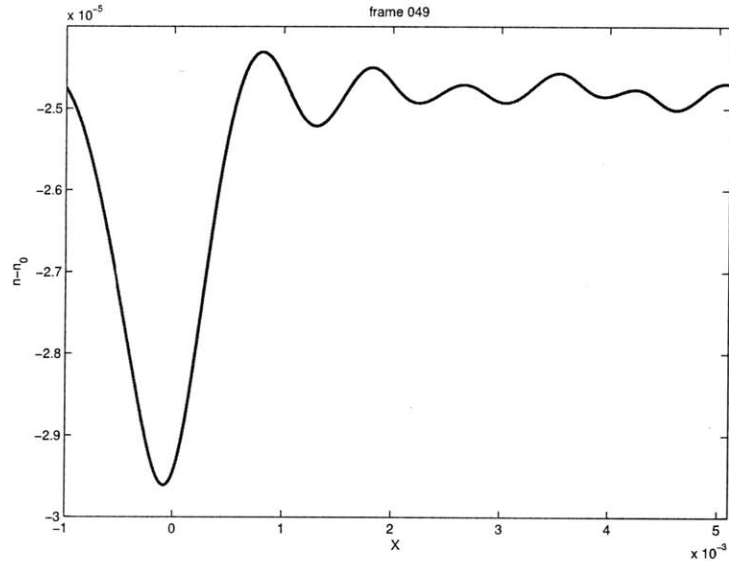
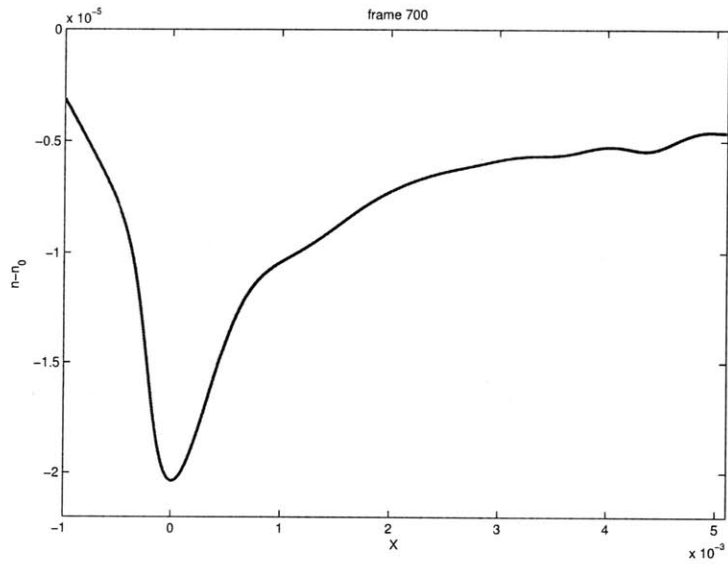


Figure 4.6: Evolution of centre-line change in refractive index with time

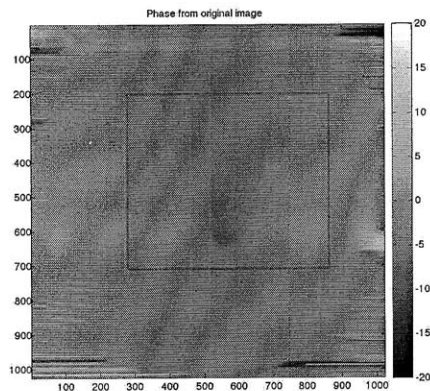


(a) At time $t = 0.1225$ s (Frame 49)

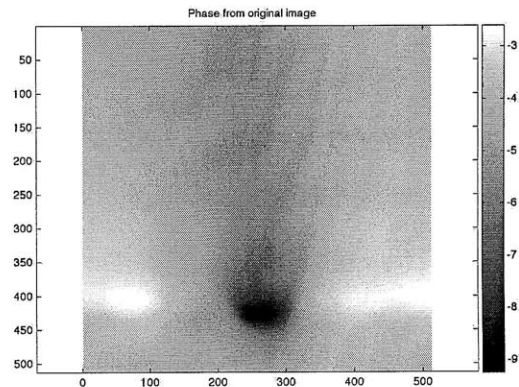


(b) At time $t = 1.75$ s (Frame 700)

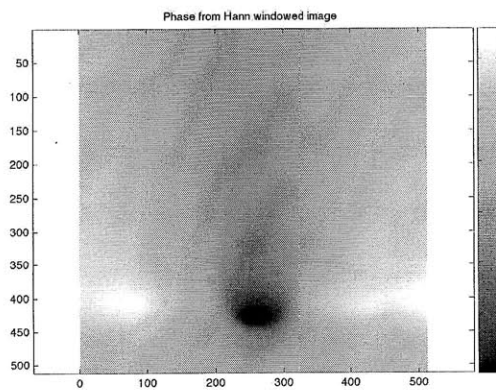
Figure 4.7: Centre-line change in refractive index at beam entry and steady state.



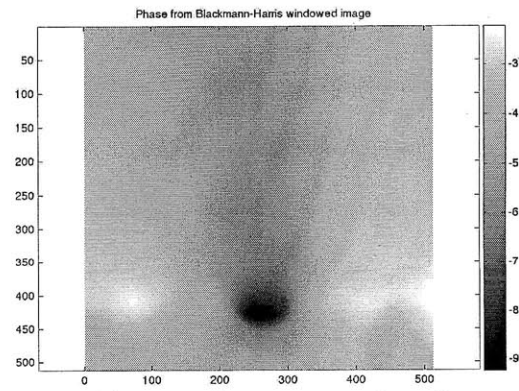
(a) Full phase (original image)



(b) Phase (original image)



(c) Phase (*Hanned*)



(d) Phase (*Blackmann-Harris*)

Figure 4.8: Phase difference due to laser heating - comparing original image data with *Hanning* and *Blackmann-Harris* windowed image.

To compare the phase predicted using this method, a centre-line for the beam is defined as earlier. Here it corresponds to column 557 of the image matrix and the beam centre is pixel (557, 626). The change in refractive index on this centre-line is then estimated. Since the camera pixel size is $12\mu\text{m}$, converting it to spatial co-ordinates (m), the change in centre-line refractive index is shown in *Figure 4.9*. It can be seen that for the area near the pump beam, the original data gives results comparable to the windowed images. The change in refractive index around the beam using the Fourier method is shown in *Figure 4.10-a*.

Next, the phase is determined by PSM. As stated earlier, four interferograms with a successive phase shift of $\pi/4$ are recorded both for the initial stage (before pump beam is incident) and the steady state. The initial stage image set gives the phase introduced by the experimental setup - the spurious phase; which on subtraction from the final stage phase, gives the phase difference due to heating. The phase again is modulo 2π and an unwrapping algorithm is applied. The change in refractive index using *Equation 4.3.1* for the region around the beam is shown in *Figure 4.10-b*.

4.4 Comparison with Simulations

For the 120mW pump laser passing through the Toluidine Blue sample, the change in refractive index using the uniform line source model of *Section 3.2* is evaluated. This is shown in *Figure 4.11*. The centre-line change in

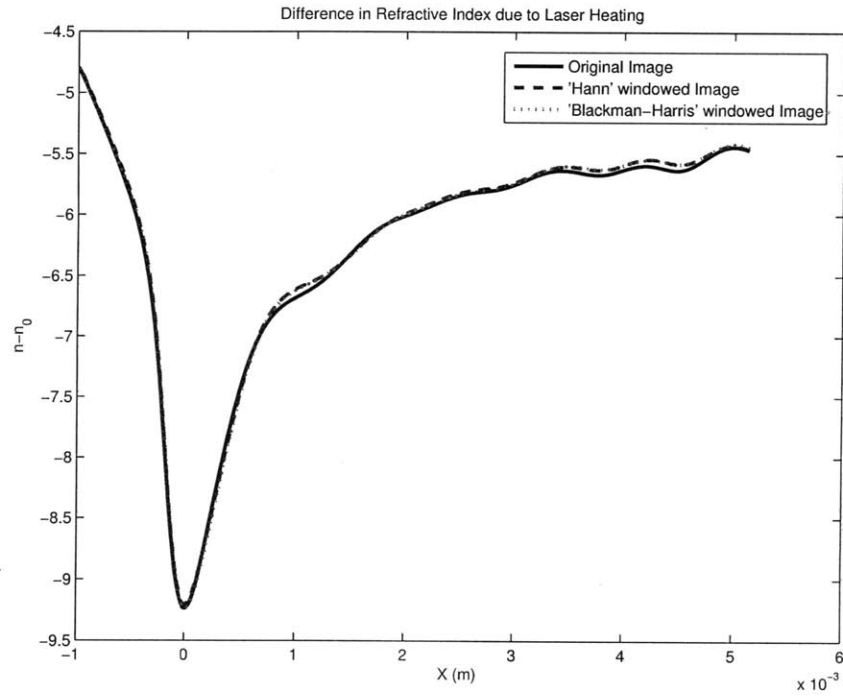


Figure 4.9: Comparing the centre-line refractive index change from Fourier Method analysis of original image with *Hann* and *BlackmanHarris* windowed images.

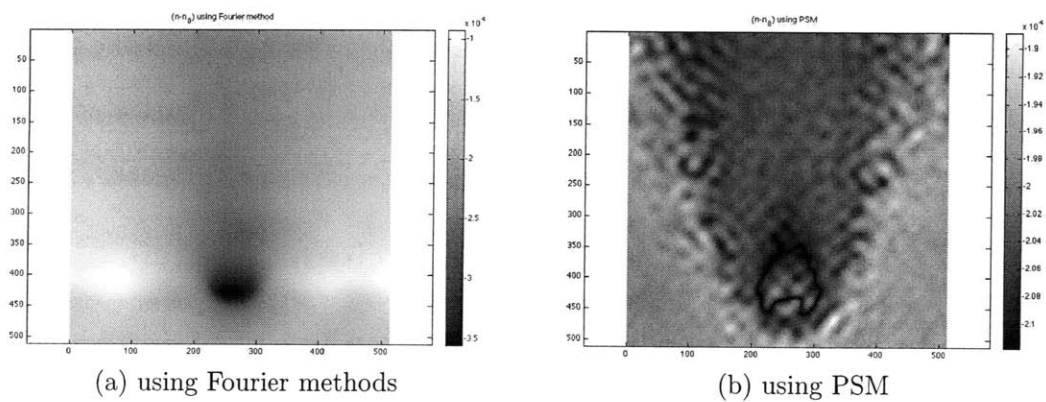


Figure 4.10: Change in refractive index around the beam using Fourier method and PSM.

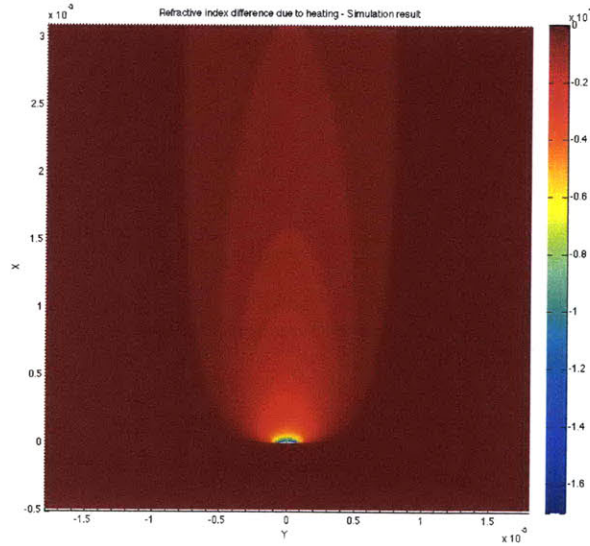


Figure 4.11: Simulation result for change in refractive index (uniform line source model).

refractive index is then compared with the experimental results and is shown in *Figure 4.12*. The pump beam has a spot size of about 0.8mm and it can be seen that the change in refractive index for simulation and experiments (Fourier method) are of the same order of magnitude around the upper rim of the beam spot and away from it. Due to the finite size of the beam spot, there is a change in refractive index below the beam centre as well. This too is approximately of the same order of magnitude as that above the origin. This would suggest a *flattened top* deformation, as predicted in *Section 3.2*, of a circular ray grid traveling through such an index distribution; not just above the beam centre but also below it. Also, the faster approach to ambient refractive index below the beam suggests that the primary mode

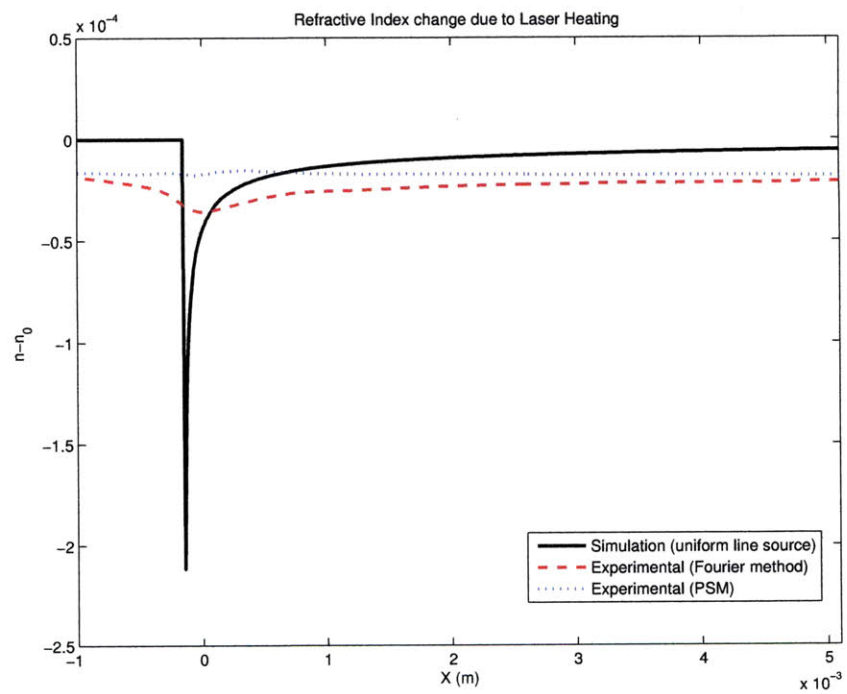


Figure 4.12: Comparing the centre-line refractive index change estimated by simulations with the experimental results (spatial distance units in m).

of heat transfer here is conduction, and a conduction model could be used to determine the index profile in this region. The phase evaluated through PSM is similar to the phase calculated by Fourier method with most deviation being at the beam location. This appears to be due to the fringes being not well defined in this region - as can be seen in the closeup images in *Figure 4.2*. The intensity at this location is smudged and possibly leads to the error in phase calculation.

The phase map in *Figure 4.8-a* shows the formation of an upward plume, characteristic of free convection flows. It is seen here that the extent of disturbance in the horizontal direction is smaller than in the vertical direction (gravity). This supports the assumption of a boundary layer formation and the approximations made thereof.

4.5 Dye Alternatives

Similar to the case of Toluidine Blue sample, the thermal lensing of an aqueous solution of Malachite Green was visualized with the setup. Defining the centre-line as earlier, the steady state change in refractive index along this centre-line is shown for both the samples in *Figure 4.13*. The change in refractive index is of the same order of magnitude for both the samples, but the profile is flattened out for Malachite Green. Also, the refractive index change at the beam centre is lower for Malachite Green than for Toluidine Blue. This is because the wavelength of pump beam is towards the lower

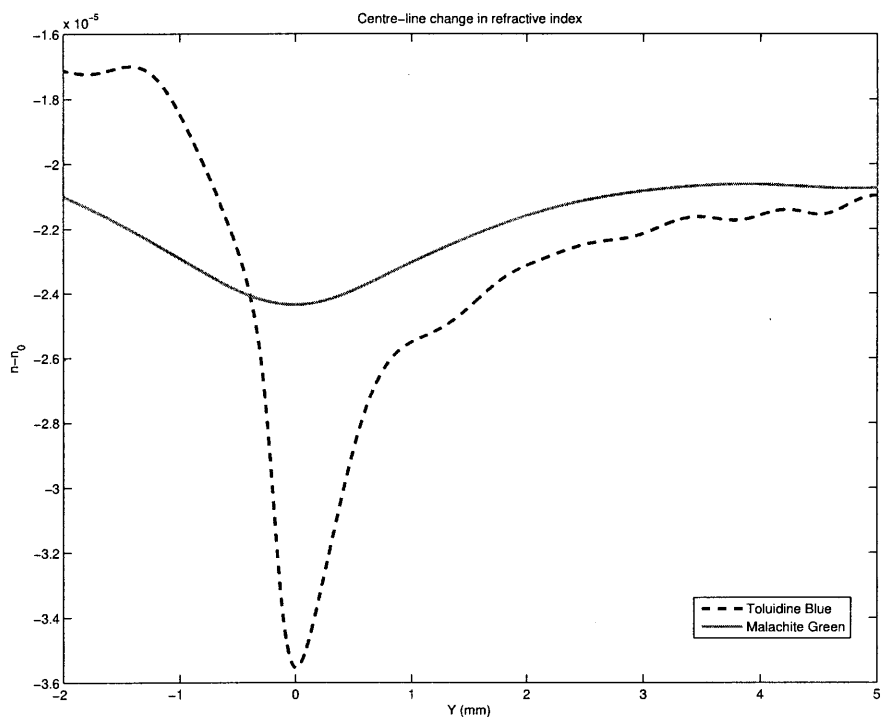


Figure 4.13: Comparing the centre-line change in refractive index for Toluidine Blue and Malachite Green at steady state.

extreme of the absorption band for Malachite Green.

Depending on the wavelength of the pump beam, different dyes could be used to visualize the thermal lensing effect. As stated earlier, the reason for using an aqueous solution is to enable increased absorption of the laser energy. The concentration of the samples however is low and hence the properties of water are taken for calculations of change in refractive index. For a pump beam in the green wavelength, Toluidine Blue or Malachite Green are good options. The response of Toluidine Blue was seen to be better at the 543nm

pump beam. With a pump beam in the green wavelength domain, aqueous solutions of Methyl Red, Safranin or Cobalt Sulphate are good options. Similar experiments showed Methyl Red to be the most responsive.

Chapter 5

Conclusion

The interaction of a high energy laser beam traveling through a medium may cause changes in the intensity distribution and path direction due to the accompanying refractive index variation. With increasing prevalence of high energy light beams, in applications where it is desired to know the peak intensity on target (for example in solar power plants) - it is important to know the beam evolution. Due to the high nonlinearity of this phenomenon, the subject matter is also of theoretical importance. The influence of self-induced convection on the propagation of a laser beam through a fluid medium was investigated in this thesis.

For the case of a beam traveling in a direction opposite to gravity (vertical beam configuration) in quiescent water at ambient conditions, two models were examined. First, the laser beam was approximated to be a line source

of equivalent power and a similarity solution for the convection field was employed. The integral method gave the temperature profile and the resulting spatial refractive index distribution. Ray evolution through such a distribution was evaluated under the Hamiltonian formulation of geometrical optics. The second model considered the finite spatial extent of the beam intensity profile to determine the refractive index distribution. Ray paths were then predicted based on the Hamiltonian formulation. Both models suggest the formation of a caustic with the densing of rays along a circle, as the rays propagate; in this case referred to as the *thermal ring*.

The propagation of a horizontal laser beam, with gravity acting in a direction perpendicular to the plane of propagation, was modelled considering the beam to be a linear energy source suspended in water. This case is more complex than the vertical beam propagation due to asymmetry of the convection flow; and forms the main part of this thesis. First, the linear source was considered to be of uniform strength along its length and a similarity solution gave the temperature profile. The resulting refractive index distribution gives the behaviour of light rays. It was seen that if at entry, the distribution of rays was along a circle; with propagation in the medium, the rays redistribute to form a flattened top (*Figure 3.7*). The extent of deformation of a circular grid changes with grid radius, and this leads to a densing of rays at two locations and suggests the formation of a caustic (*Figure 3.8*). This is similar to the crescent shape formation for the forced convection case (*Figure 3.3*) which concerns a Gaussian beam traveling in a medium with a

cross-flow, in the sense that the deformation is in a direction opposite to the fluid flow. The next model considers the laser beam to be a linear source of decreasing intensity. Here too, the circular grids of rays evolve leading to densing of rays at two locations above the beam centre. However, this gives only a qualitative estimation as the similarity solution employed to calculate the refractive index profile is valid only for grids located far from the beam centre.

The validity of uniform line source model for a horizontal laser beam was confirmed by interferometric visualization of the thermal lensing effect produced by a 120mW laser beam passing through a liquid sample. The change in refractive index due to laser heating was found to be of the same order of magnitude as that predicted by simulation with equivalent parameters. The phase map around the laser beam distinctly showed the formation of a boundary layer strengthening the approximations. Thus, if dissipation of energy due to absorption by the fluid is not high - so as to consider the beam to be of constant strength along the beam propagation, the uniform line source model is a reasonable approximation to determine the evolution of such a laser beam.

Future Directions

The similarity solution approach to solving the Navier-Stokes equation help reduce the PDEs to ODEs and thus simplifies arriving at a solution. The case

of a horizontal laser beam propagating through a medium was approximated with the line source model, where the spatial extent of intensity generation is ignored. If the intensity term is considered, similarity function definitions need to be defined as per the requirements outlined in *Appendix B*. The similarity solution however is valid at distances away from the beam centre. Hence, to have an accurate behaviour of the beam evolution, a full solution to the Navier-Stokes needs to be attempted. One approach is to employ a finite element/ finite volume method solution to find the temperature profile. Another approach is to solve the coupled nonlinear PDEs using techniques like perturbation theory or homotopy analysis. Homotopy analysis is a relatively new analytic method for nonlinear problems, with the solution valid even in presence of strong nonlinearity [69, 70]. This has been applied to solving convection problems with increased accuracy [71]. Instabilities like turbulence of the flow would also need to be considered with increasing laser powers. The problem of influence of self-induced convection on propagation of a high energy laser thus presents immense theoretical significance in the nonlinear interactions between the beam and medium.

The geometrical treatment of beam propagation is limited to predicting the behaviour up to formation of caustics. A wave theory approach can explain beam propagation beyond caustic formation and also consider the scattering phenomenon. For experimental visualization of thermal lensing, techniques like tomography [72] can be used for better results - especially in the case where high absorption of beam energy by the fluid causes a 3D flow and

temperature field. The accurate visualization of such a fast transient phenomenon will support the theoretical explanation and the assumptions made thereof.

Appendix A

Livingston Parameter β

The theory developed by Livingston [1] is for a high energy beam traveling through air. To extend it to a fluid medium, the heat balance equation (*Equation 6* [1]) is examined. If the local temperature difference is δT , then

$$\left(\mathbf{V} \cdot \nabla_{\perp} - a \nabla_{\perp}^2\right) \delta T = \frac{\alpha}{\rho C_p} I, \quad (\text{A.1})$$

where the symbols are as used in the reference. To a first order approximation, $\delta n = (dn/dT) \delta T$ so that

$$\left(\mathbf{V} \cdot \nabla_{\perp} - a \nabla_{\perp}^2\right) \delta n = \frac{\alpha (dn/dT)}{\rho C_p} I = -\frac{1}{2} \Xi I \quad (\text{A.2})$$

where Ξ determines the parameter β used to evaluate intensity. Thus, for a fluid medium the parameter of interest (called the Livingston parameter here) is

$$\beta = \frac{I_0 d_0}{2V} \Xi = -\frac{\alpha I_0 d_0}{\rho C_p V} \left(\frac{dn}{dT}\right). \quad (\text{A.3})$$

Appendix B

Convection ODEs and Approximation Validity

The approach of assuming a similarity solution to reduce the complexity of the PDEs by converting to a system of ODEs is standard. Starting with the three equations of mass continuity, momentum balance and heat balance for a fluid under the boundary layer formulation and Boussinesq approximation, for a 2D flow, we have from *Section 1.3*

$$\frac{\partial u}{\partial x} + \frac{\partial v}{\partial y} = 0, \quad (\text{B.1})$$

$$u \frac{\partial u}{\partial x} + v \frac{\partial u}{\partial y} = g\theta + \nu \frac{\partial^2 u}{\partial y^2}, \quad (\text{B.2})$$

$$u \frac{\partial \theta}{\partial x} + v \frac{\partial \theta}{\partial y} = \alpha \frac{\partial^2 \theta}{\partial y^2} + \frac{\alpha_a \beta}{\rho C_p} I \quad (\text{B.3})$$

where $\theta = \beta \Delta T = \beta(T - T_\infty)$ is the excess temperature and I is the intensity of the laser beam which acts as the heat generation term. Assume that a similarity solution exists. Define a similarity parameter $\xi = y/a(x)$, and a function definition for the stream function as $\psi = \nu h(x)f(\xi)$ and $\theta = H(x)F(\xi)$. Take

derivatives and, dropping variables¹ the derivatives are:

$$\xi_y = 1/a; \xi_x = -\xi a'/a$$

$$u = \psi_y = \frac{\nu h}{a} f'; v = -\psi_x = -\nu \left(h' f - \frac{\xi h a'}{a} f' \right)$$

$$u_x = \nu \left[\frac{h'}{a} f' + \left(-\xi \frac{a' h}{a^2} \right) f'' - \left(\frac{h a'}{a^2} \right) f \right]; u_y = \nu \frac{h}{a^2} f''; u_{yy} = \nu \frac{h}{a^3} f'''$$

$$\theta_x = H' F - \frac{\xi a' H}{a} F'; \theta_y = \frac{H}{a} F'; \theta_{yy} = \frac{H}{a^2} F''$$

Using these, the continuity equation *B.1* is satisfied by definition and the momentum equation equation *B.2* and energy equation *B.3* are, respectively

$$\nu^2 \frac{h}{a^3} \left[f''' + (h a' - h' a) (f')^2 + h' a (f f'') + \frac{g a^3}{\nu^2 h} \theta \right] = 0, \quad (\text{B.4})$$

$$\alpha \frac{H}{a^2} \left[F'' - Pr \left(\frac{a h H'}{H} \right) f' F + Pr (a h') f F' + \frac{\alpha_a \beta}{\alpha \rho C_p} \frac{a^2}{H} I \right] = 0. \quad (\text{B.5})$$

Thus for converting the PDEs to ODEs, the coefficients of the following equations should be independent of x and the equations to be satisfied are:

$$f''' + (h a' - h' a) (f')^2 + h' a (f f'') + \left(\frac{g a^3 H}{\nu^2 h} \right) F = 0 \quad (\text{B.6})$$

$$F'' - Pr \left(\frac{a h H'}{H} \right) f' F + Pr (a h') f F' + \left(\frac{\alpha_a \beta}{\alpha \rho C_p} \frac{a^2}{H} \right) I = 0 \quad (\text{B.7})$$

Using the function definitions from [43] and as mentioned in *Section 3.2.2*, the last term in *Equation B.7* is

$$\left(\frac{\alpha_a \beta}{\alpha \rho C_p} \frac{a^2}{H} \right) I = \frac{\alpha_a}{\rho C_p \alpha \theta_l} \left(\frac{\nu^2}{g \beta \theta_l} \right)^{-1/5} x^{7/5} I. \quad (\text{B.8})$$

For the simulation parameters used, the value of this term with respect to maximum intensity I_0 for a Gaussian distribution with spot size of 2mm is shown

¹Henceforth functions a, h, H and their derivatives are understood to be functions of x only, whereas derivatives of ψ, θ etc. are with respect to ξ

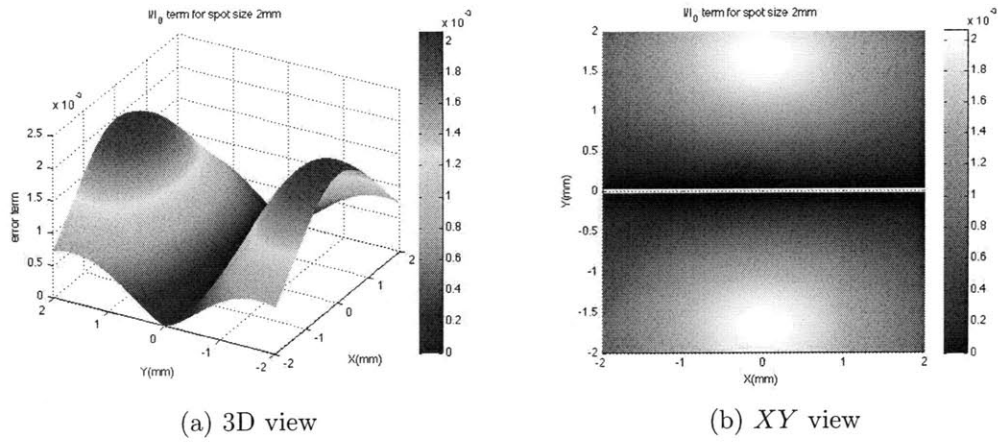


Figure B.1: The error term

in *Figure B.1*. This gives an idea of the error distribution when neglecting the intensity term in the uniform horizontal line source model.

Bibliography

- [1] P. M. Livingston, "Thermally Induced Modifications of a High Power cw Laser Beam", *Appl. Opt.*, **10**(2), pp. 426-436 (1971).
- [2] D. C. Smith, "Thermal Defocusing of CO₂ Laser Radiation in Gases", *IEEE J. Quantum Electron.*, **QE-5**(12), pp. 600-607 (1969).
- [3] D. C. Smith and F. G. Gebhardt, "Saturation of the Self-Induced Thermal Distortion of Laser Radiation in a Wind", *Appl. Phys. Lett.*, **16**(7), pp. 275- 278(1970).
- [4] F. G. Gebhardt and D. C. Smith, "Self-Induced Thermal Distortion in the Near Field for a Laser Beam in a Moving Medium", *IEEE J. Quantum Electron.*, **QE-7**(2), pp. 63-73 (1971).
- [5] J. N. Hayes, "Thermal Blooming of Laser Beams in Fluids", *Appl. Opt.*, **11**(2), pp. 455- 461(1972).
- [6] S. A. Akhmanov, D. P. Krindach, A. V. Migulin, A. P. Sukhorukov and R. V. Khokhlov, "Thermal Self-Actions of Laser Beams", *IEEE J. Quantum Electron.*, **QE-4**(10), pp. 568-575 (1968).
- [7] P. V. Avizonics, C. B. Hogge, R. R. Butts and J. R., Kenemuth, "Geometric Optics of Thermal Blooming in Gases. Part 1", *Appl. Opt.*, **11**(3), pp. 554-564 (1972).
- [8] L. R. Bissonnette, "Thermally Induced Nonlinear Propagation of a Laser Beam in an Absorbing Fluid Medium", *Appl. Opt.*, **12**(4), pp. 719-728 (1973).
- [9] J. R. Whinnery, D. T. Miller and F. Dabby, "Thermal Convection and Spherical Aberration Distortion of Laser Beams in Low-Loss Liquids", *IEEE J. Quantum Electron.*, (1967).
- [10] R. Anthore, P. Flament, G. Gouesbet, M. Rhazi and M. E. Weill, "Interaction between a laser beam and some liquid media", *Appl. Opt.*, **21**(1), pp. 2-4 (1982).
- [11] A. N. Kucherov, "Strong thermal self-action of a laser beam in gases and liquids", *J. Experimental and Theoretical Phys.*, **89**(1), pp. 56-69 (1999).

- [12] J. N. Hayes, P. B. Ulrich, and A. H. Aitken, "Effects of the Atmosphere on the Propagation of 10.6- μ Laser Beams", *Appl. Opt.*, **11**(2), pp. 257- 260 (1972).
- [13] F. G. Gebhardt, "High power laser propagation", *Appl. Opt.*, **15**(6), pp. 1479-1493 (1976).
- [14] M. H. Mahdleh and B. Loftl, "Two-dimensional simulation of thermal blooming effects in ring pattern laser beams", *Opt. Engg.*, **44**((9), (2005).
- [15] T. Sekiguchi and K. B. Wolf, "The Hamiltonian formulation of optics", *Am. J. Phys.* **55**(9), pp. 830-835 (1987).
- [16] K. B. Wolf, *Geometric Optics on Phase Space*, Springer (2004).
- [17] M. Born and E. Wolf, *Principles of optics: Electromagnetic Theory of Propagation, Interference and Diffraction of Light*, Cambridge University Press, Edition 7 (1999).
- [18] P. K. Kundu and I.M. Cohen, *Fluid Mechanics*, Elsevier, Edition 3 (2005).
- [19] B. Gebhart, Y. Jaluria, R. L. Mahajan and B. Sammakia, *Buoyancy-Induced Flows and Transport*, Hemisphere Publishing Corporation, Reference Edition (1988).
- [20] L. Crescentini and G. Fiocco, "Interferometric investigations of convection around cylinders at small Grashof numbers", *Appl. Opt.*, **29**(10), pp. 1490-1495 (1990).
- [21] S. De Nicola, A. Finizio, P. Ferraro and G. Pierattini, "An interferometric technique based on Fourier fringe analysis for measuring the thermo-optic coefficients of transparent materials", *Opt. Commun.*, **159**, pp. 203-207 (1999).
- [22] D. Naylor, "Recent developments in the measurement of convective heat transfer rates by laser interferometry", *Int. J. Heat and Fluid Flow*, **24**, pp. 345-355 (2003).
- [23] M. Goharkhah, M. Ashjaee and K. Madanipour, "Investigation of the accuracy of different methods of interferogram analysis for calculation of local free convection heat transfer coefficient on axisymmetric objects", *Experimental Thermal and Fluid Science*, **33**, pp. 1188-1196 (2009).
- [24] L. Hesselink, "Digital Image Processing in Flow Visualization", *Ann. Rev. Fluid Mech.*, **20**, pp. 421-485 (1988).
- [25] P. Hariharan, *Basics of Interferometry*, Elsevier, Edition 2 (2007).
- [26] M. Takeda, I. Hideki and S. Kobayashi, "Fourier-transform method of fringe-pattern analysis for computer-based topography and interferometry", *J. Opt. Soc. Am.*, **72**(1), pp. 156-160 (1982).

- [27] W. W. Macy, "Two-dimensional fringe-pattern analysis", *Appl. Opt.*, **22**(23), pp. 3898-3901 (1983).
- [28] K. A. Nugent, "Interferogram analysis using an accurate fully automatic algorithm", *Appl. Opt.*, **24**(18), pp. 3101-3105 (1985).
- [29] D. J. Bone, H. A. Bachor, and R. J. Sandeman, "Fringe-pattern analysis using a 2-D Fourier transform", *Appl. Opt.*, **25**(10), pp. 1653-1660 (1986).
- [30] T. Kreis, "Digital holographic interference-phase measurement using the Fourier-transform method", *J. Opt. Soc. Am. A*, **3**(6), pp. 847-855 (1986).
- [31] C. Roddier and F. Roddier, "Interferogram analysis using Fourier transform techniques", *Appl. Opt.*, **26**(9), pp. 1668-1673 (1987).
- [32] M. Kujiawinska and J. Wójciak, "High Accuracy Fourier Transform Fringe Pattern Analysis", *Optics and Lasers in Engineering*, **14**, pp. 325-339 (1991).
- [33] C. Gorecki, "Interferogram analysis using a Fourier transform method for automatic 3D surface measurement", *Pure Appl. Opt.* **1**, pp. 103-110 (1992).
- [34] D. Malacara, M. Servín and Z. Malacara, *Interferogram Analysis for Optical Testing*, Taylor & Francis, Edition 2 (2005).
- [35] C. M. Vest, "Analysis of laser-induced convection in unconfined fluids and in vertical cylinders", *The Phys. of Fluids*, **17**(11), pp. 1945-1950 (1974).
- [36] S. H. Lehnigk, and B. Steverding, "High-intensity light propagation and induced natural laminar flow", *J. Fluid Mech.*, **66**(4), pp. 817-829 (1974).
- [37] A. N. Kucherov, "Transient thermal blooming of a vertical laser beam", *Quantum Electron.*, **27**(2), pp. 176-181 (1997).
- [38] I. Thormählen, J. Straub and U. Griguli, "Refractive Index of Water and Its Dependence on Wavelength, Temperature and Density", *J. Phys. Chem. Ref. Data*, **14**(4), pp. 936 (1985).
- [39] C. A. Carter and J. M. Harris, "Comparison of models describing the thermal lens effect", *Appl. Opt.*, **23**(3), pp. 476- 481(1984).
- [40] L. J. Crane, "Thermal Convection from a Horizontal Wire", *Z. Angew. Math. Phys.*, **10**, pp. 453-460 (1959).
- [41] Chia-Shun Yih, "Free convection due to a line source of heat", *Trans. Am. Geophys. Un.*, **33**, pp. 669-672 (1962).

- [42] D. B. Spalding and R. G. Cruddace, "Theory of the steady laminar buoyant flow above a line heat source in a fluid of large Prandtl number and temperature-dependent viscosity", *Int. J. Heat Mass Transfer*, **3**, pp. 55-59 (1961).
- [43] T. Fujii, "Theory of the steady laminar natural convection above a horizontal line heat source and a point heat source", *Int. J. Heat Mass Transfer*, **6**, pp. 597-606 (1963).
- [44] R. J. Forstrom and E. M. Sparrow, "Experiments on the buoyant plume above a heated horizontal wire", *Int. J. Heat Mass Transfer*, **10**, pp. 321-331 (1967).
- [45] R. S. Brand and F. J. Lahey, "Heater laminar vertical jet", *J. Fluid Mech.*, **29**, pp. 305-315 (1967).
- [46] T. Fujii, I. Morioka and H. Uehara, "Buoyant plume above a horizontal line heat source", *Int. J. Heat Mass Transfer*, **16**, pp. 755-768 (1973).
- [47] B. Gebhart, L. Pera and A. W. Schorr, "Steady laminar natural convection plumes above a horizontal line heat source", *Int. J. Heat Mass Transfer*, **13**, pp. 161-171 (1970).
- [48] H. K. Kuiken and Z. Rotem, "Asymptotic solution for plume at very large and small Prandtl numbers", *J. Fluid Mech.*, **45**(3), pp. 585-600 (1971).
- [49] C. M. Vest and M. L. Lawson, "Onset of convection near a suddenly heated horizontal wire", *Int. J. Heat Mass Transfer*, **15**, pp. 1281-1283 (1972).
- [50] C. A. Hieber and E. J. Nash, "Natural convection above a line heat source: higher-order effects and stability", *Int. J. Heat Mass Transfer*, **18**, pp. 1473-1479 (1975).
- [51] A. Liñán and V. N. Kurdyumov, "Laminar free convection induced by a line heat source, and heat transfer from wires at small Grashof numbers", *J. Fluid Mech.*, **362**, pp. 199-227 (1998).
- [52] M. Duluc, S. Xin and P. Le Quéré, "Transient natural convection and conjugate transients around a line heat source", *Int. J. Heat Mass Transfer*, **46**, pp. 341-354 (2003).
- [53] O. G. Martynenko and V. N. Korovkin, "Toward calculation of free-convective motion of liquid over a linear heat source", *J. Engg. Phys. and Thermophysics*, **80**(4), pp. 708-713 (2007).
- [54] M. Duluc, S. Xin, F. Lusseyran and P. Le Quéré, "Numerical and experimental investigation of laminar free convection around a thin wire: Long time scalings and assessment of numerical approach", *Int. J. Heat Fluid Flow*, **29**, pp. 1125-1138 (2008).

- [55] R. D. Boyd, "Natural convection induced by a horizontal laser beam", PhD. Thesis, University of Michigan (1976).
- [56] R. D. Boyd and C. M. Vest, "Onset of convection due to horizontal laser beams", *Appl. Phys. Lett.*, **26**(6), pp. 287-288 (1975).
- [57] R. D. Boyd and C. M. Vest, "Laminar natural convection above a horizontal laser beam", *Int. J. Heat Mass Transfer*, **24**(4), pp. 685-694 (1981).
- [58] J. P. Gordon, R. C. C. Leite, R.S. Moore, S.P.S. Porto and J.R. Whinnery, "Long-transient Effects in Lasers with Inserted Liquid Samples", *J. Appl. Phys.*, **36**(1), pp. 3-8 (1965).
- [59] V. P. Kozich, A. Marcano, F. E. Hernandez and J. A. Castillo, "Dual-beam timeresolved Z-scan in liquids to study heating due to linear and nonlinear light absorption", *Appl. Spectrosc.*, **48**, pp.1506-1512 (1994).
- [60] A. Marcano, C. Loper and N. Meliechi, "Pump-probe mode-mismatched thermal-lens Z scan", *J. Opt. Soc. Am. B*, **19**(1), pp. 119-124 (2002).
- [61] J. Shen, A. J. Soroka and R. D. Snook, "A model for cw laser induced mode-mismatched dual-beam thermal lens spectrometry based on probe beam profile image detection", *J. Appl. Phys.*, **78**(2), pp. 700-708 (1995).
- [62] R. Escalona and C. Rosi, "Space and time characterization of a thermal lens using an interferometric technique", *Opt. Eng.*, **38**(9), pp. 1591-1595 (1999).
- [63] R. Escalona, "Study of axial absorption in liquids by interferometry", *J. Opt. A: Pure Appl. Opt.*, **5**, pp. S355-S360 (2003).
- [64] L. Rodriguez and R. Escalona, "Fourier transforms method for measuring thermal lens induced in diluted liquid samples", *Opt. Commun.*, **277**, pp. 57-62 (2007).
- [65] R. Escalona, "Study of a convective field induced by thermal lensing using interferometry", *Opt. Commun.*, **281**, pp. 388-394 (2008).
- [66] L. A. Ageev, M. G. Kuleva and R. G. Yarovaya, "A simple demonstration experiment in nonlinear optics (Thermal defocusing of laser radiation)", *Sov. Phys. Usp.*, **30**(3), pp. 284-285 (1987).
- [67] J. Lindsey, "Malachite Green", <http://omlc.ogi.edu/spectra/PhotochemCAD/html/malachiteGreen.html> [accessed 27 April 2010].
- [68] M. Abramowitz and M. W. Davidson, "Molecular Expressions Microscopy Primer: Photomicrography - Absorption Characteristics of Stains for Black & White Photomicrography", <http://micro.magnet.fsu.edu/primer/photomicrography/bw-stainchart.html> [accessed 27 April 2010].

- [69] S. Liao, "Homotopy analysis method: a new analytic method for nonlinear problems", *Appl. Mathematics and Mechanics*, **19**(10), pp. 957- 962(1998).
- [70] S. Liao, *Beyond Perturbation: Introduction to the Homotopy analysis method*, Chapman & Hall/CRC (2004).
- [71] S. Liao, J. Su and A. T. Chwang, "Series solutions for a nonlinear model of combined convective and radiative cooling of a spherical body", *Int. J. Heat Mass Transfer*, **49**, pp. 2437-2445 (2006).
- [72] Y. C. Michael and K. T. Yang, "Recent Developments in Axial Tomography for Heat Transfer and Fluid Flow Studies", *Exp. Thermal and Fluid Science*, **4**, pp. 637-647 (1991).